

Squall-Line Intensification via Hydrometeor Recirculation

ROBERT B. SEIGEL AND SUSAN C. VAN DEN HEEVER

Colorado State University, Fort Collins, Colorado

(Manuscript received 2 October 2012, in final form 29 November 2012)

ABSTRACT

Many studies have demonstrated the intimate connection between microphysics and deep moist convection, especially for squall lines via cold pool pathways. The present study examines four numerically simulated idealized squall lines using the Regional Atmospheric Modeling System (RAMS) and includes a control simulation that uses full two-moment microphysics and three sensitivity experiments that vary the mean diameter of the hail hydrometeor size distribution. Results suggest that a circulation centered at the freezing level supports midlevel convective updraft invigoration through increased latent heating. The circulation begins with hail hydrometeors that initiate within the convective updraft above the freezing level and are then ejected upshear because of the front-to-rear flow of the squall line. As the hail falls below the freezing level, the rear-inflow jet (RIJ) advects the hail hydrometeors downshear and into the upshear flank of the midlevel convective updraft. Because the advection occurs below the freezing level, some of the hail melts and sheds raindrops. The addition of hail and rain to the updraft increases latent heating owing to both an enhancement in riming and vapor deposition onto hail and rain. The increase in latent heating enhances buoyancy within the updraft, which leads to an increase in precipitation and cold pool intensity that promote a positive feedback on squall-line strength. The upshear-tilted simulated squall lines in this study indicate that as hail size is decreased, squall lines are invigorated through the recirculation mechanism.

1. Introduction

The role of the rear-inflow jet (RIJ) has been shown to be a key component in the structure and maintenance of squall lines (Smull and Houze 1987; Fovell and Ogura 1988; Lafore and Moncrieff 1989; Weisman 1992; Tao et al. 1995; Grim et al. 2009). The RIJ forms predominantly in response to midlevel horizontal pressure and buoyancy gradients. These gradients are generated by both the latent heating of the main convective updraft and the dipole of upper-level latent heating above low-level latent cooling in upshear-tilted squall lines, driving a midlevel mesolow (Brown 1979; Smull and Houze 1987; Weisman 1992; Haertel and Johnson 2000). The rear-to-front flow of the RIJ impacts squall-line intensity by 1) enhancing convective downdrafts that aid in strengthening the surface cold pool (Fovell and Ogura 1988; Weisman 1992; Tao et al. 1995); 2) transporting momentum from aloft to the surface cold pool, thereby assisting deeper lifting near the gust front (Newton 1950; Smull and Houze 1987; Lafore and Moncrieff 1989; Weisman

1992); and 3) transporting horizontal vorticity to the leading edge of upshear-tilted squall lines that have an elevated RIJ, such that it opposes the sign of horizontal vorticity within the cold pool and aids the dynamical balance between the cold pool and environmental shear (Rotunno et al. 1988; Weisman 1992, 1993). In general, the dominant communication between the RIJ and the intensity of the convective line is through the cold pool.

Studies have shown that the cold pool plays a key role in the life cycle and dynamics of squall lines (Thorpe et al. 1982; Rotunno et al. 1988, hereafter RKW88, 1990; Weisman et al. 1988, hereafter WKR88; Weisman 1992, 1993; Weisman and Rotunno 2004, hereafter WR04, 2005, hereafter WR05; Bryan et al. 2006). RKW88 proposed perhaps the most widely accepted theory for squall-line maintenance in which a balance exists between the vorticity generated within the cold pool and the environmental shear. If the vorticities are similar in magnitude but have the opposite sign, then the convective updraft remains upright, which yields the deepest lifting of environmental air and maximum system intensity. RKW88 describe this balance using a ratio between cold pool propagation speed (C) and the environmental shear (ΔU), $C/\Delta U$, which has been derived using simplifying

Corresponding author address: Robert B. Seigel, 1371 Campus Delivery Drive, Fort Collins, CO 80523.
E-mail: rseigel@atmos.colostate.edu

assumptions of the horizontal vorticity equation. However, numerous factors should be taken into consideration when using RKW88 theory for squall-line analysis, such as 1) the depth and location of the shear layer (WKR88; WR04; Stensrud et al. 2005; WR05; Coniglio et al. 2012), 2) the calculation of cold pool intensity (Stensrud et al. 2005; WR05; Bryan and Parker 2010; Coniglio et al. 2012), 3) stability layers that can interact with the cold pool dynamics (Carbone et al. 1990; Xue 2002; Seigel and van den Heever 2012a), and 4) microphysics (e.g., Fovell and Ogura 1988; Ferrier et al. 1995; Adams-Selin et al. 2013a,b; Bryan and Morrison 2012).

Numerous studies have shown the sensitivity of simulated squall lines to microphysics (Morrison et al. 2009; Bryan and Morrison 2012; Morrison et al. 2012; Van Weverberg et al. 2012) and the importance of the ice phase feeding back onto squall-line dynamics (Nicholls 1987; Fovell and Ogura 1988; McCumber et al. 1991; Tao et al. 1995; Liu et al. 1997; Adams-Selin et al. 2013a,b; Bryan and Morrison 2012). Fovell and Ogura (1988) were among the first to show that the inclusion of the ice phase resulted in a more realistic representation of an upshear-tilted squall line. Tao et al. (1995) demonstrated that the exclusion of the melting process leads to a less commonly observed unicell-type squall line, while the inclusion of the melting process strengthens the RIJ and forces the squall line to tilt upshear as a multicellular system. Bryan and Morrison (2012) found that a numerically simulated squall line with hail microphysics and fine horizontal grid spacing best reproduced an observed squall line. A dependency on melting rates has also been found to impact squall-line structure and the subsequent bow-echo formation, as shown by Adams-Selin et al. (2013b) in which faster melting rates yield stronger rear-inflow and more frequent, more intense bow echoes. From these studies, it can be seen that there is an intricate balance between the microphysics, which is responsible for latent heating and the associated buoyancy, and the dynamics of the squall line itself. Through both hydrometeor loading and the vertical distribution of latent heating, the behavior of a squall line is subject to changes in the microphysics.

The research presented in this paper attributes another role to the RIJ of a squall line through microphysical influences. Using simulations of an idealized squall line with a convection-resolving model (CRM), it is found that for an upshear-tilted squall line the RIJ can play an integral role in recycling hail and rain hydrometeors that fall out from the updraft back into the main convective updraft, thereby locally enhancing latent heating and generating greater positive buoyancy. To assess the

importance of this recirculation mechanism, sensitivity experiments are performed that vary the mean diameter of the hail hydrometeor size distribution, which can occur in reality via mechanisms such as aerosol ingestion (Tulet et al. 2010; Seigel and van den Heever 2012b) and subsequent microphysical processing (e.g., van den Heever et al. 2006, 2011; Storer et al. 2010; Lebo and Seinfeld 2011). The following section describes the model used for this study and the experimental design. Section 3 presents the results of this mechanism based on the control simulation, and section 4 presents and discusses the results of the sensitivity experiment. Finally, a summary is provided in section 5.

2. Methods

a. Model description

The numerical model that was used for the squall-line simulations analyzed here is the nonhydrostatic Regional Atmospheric Modeling System (RAMS; Pielke et al. 1992; Cotton et al. 2003; Saleeby and Cotton 2004). As microphysics has been shown to be an important factor in correctly reproducing squall lines (Tao et al. 1995; Fovell et al. 2006; Adams-Selin et al. 2013a,b; Bryan and Morrison 2012; Morrison et al. 2012; Van Weverberg et al. 2012), RAMS is appropriate for this numerical study given its sophisticated bin-emulating two-moment bulk microphysical parameterization scheme that prognoses mass-mixing ratio and number concentration for eight hydrometeor species (cloud droplets, drizzle, rain, pristine ice, snow, aggregates, graupel, and hail) (Meyers et al. 1997; Cotton et al. 2003; Saleeby and Cotton 2004). The representation of numerous hydrometeor species that all conform to a generalized gamma distribution (Flatau et al. 1989; Verlinde et al. 1990) helps to resemble the continuous spectrum of hydrometeors within the atmosphere. Each hydrometeor distribution has its own mass and terminal velocity power-law relationships as a function of diameter that allows mass stratification from sedimentation (Walko et al. 1995). Other schemes used in the simulations are radiative boundary conditions (Klemp and Wilhelmson 1978) for all four lateral boundaries, a Rayleigh damping layer within the top six levels of the model domain, the Smagorinsky (1963) turbulence closure scheme, and Harrington (1997) two-stream radiation (Lilly 1962; Hill 1974). The Land Ecosystem–Atmosphere Feedback model (LEAF3; Walko et al. 2000) is also used to simulate realistic drag and surface fluxes over a land surface of bare soil. Coriolis forcing is excluded to keep the squall-line flow predominantly perpendicular to the meridionally oriented cold pool.

b. Experimental design

In this study, four idealized simulations are performed of a continental-type squall line to investigate a microphysical recirculation mechanism that is hypothesized to enhance squall-line intensity. All simulations are performed in three dimensions with a constant horizontal grid spacing of 500 m and a 65-level stretched vertical grid from 50 to 500 m. While a horizontal grid spacing of 100 m may be more appropriate for this study (Bryan et al. 2003), the detailed microphysical scheme employed herein is simply too computationally expensive to perform at such resolutions for squall lines. The model domain covers a volume of $500 \times 150 \times 26 \text{ km}^3$ in the zonal, meridional, and vertical directions, respectively. The time step used is 3 s and time integration is performed for 7 h nocturnally, as this is the peak occurrence time of mesoscale convective systems (MCSs) (Laing and Fritsch 1997; Anderson and Arritt 1998; Jirak et al. 2003). For cloud and ice nucleation in all simulations, background concentrations of 600 cm^{-3} and $10\,000 \text{ kg}^{-1}$ are used for aerosol species that can be activated as cloud condensation nuclei (CCN) and ice nuclei (IN), respectively, and are typical amounts for continental aerosol regimes (DeMott et al. 2003; Ward and Cotton 2011).

The model setup used here is similar to other previous idealized studies (Trier et al. 1997; Fierro et al. 2008; Morrison et al. 2009). The model is initialized with horizontally homogenous temperature and moisture profiles (Fig. 1) following Weisman and Klemp (1982); however, the boundary layer temperature profile has been adjusted to that of a well-mixed boundary layer (constant potential temperature) to better represent surface-based lifting (i.e., neutral buoyancy of dry surface air parcels within the boundary layer). The shear profile used for this analysis linearly increases from 0 to 12.5 m s^{-1} in the lower 2.5 km (Fig. 1) and has been chosen to closely match a $C/\Delta U$ of approximately 1, which will be discussed further in section 4. This shear value and depth is within the range used by previous studies (Weisman 1992, 1993; WR04; Frame and Markowski 2006; Bryan et al. 2007). The squall lines are initiated using a 4-km-deep, -6-K line thermal resting on the surface, representing a cold pool, and contains random embedded $-0.1 \leq \theta \leq 0.1 \text{ K}$ potential temperature (θ) perturbations to initiate three-dimensional motions. All of the analysis presented here is from 3 h after initialization to allow for sufficient spinup of each squall line and to ensure they are self-sustaining.

The squall-line recirculation mechanism that is discussed in section 3 is highly dependent on the size of the hail hydrometeors and their location relative to the

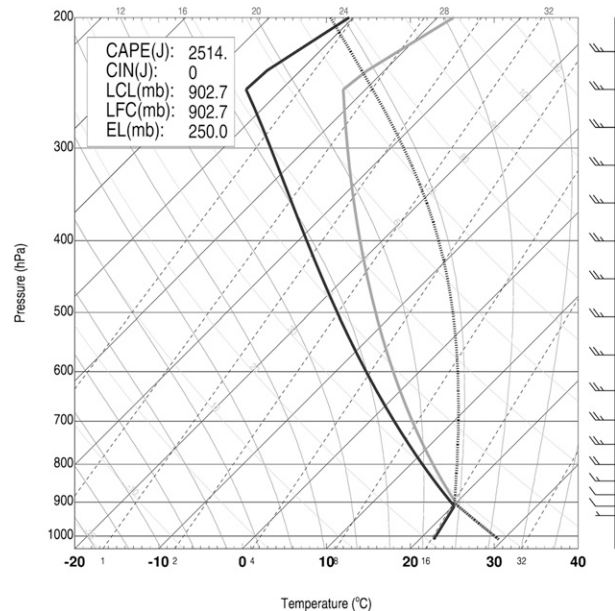


FIG. 1. Horizontally homogeneous environmental conditions initialized for the squall line. The thick gray line is the temperature profile and the thick black is the moisture profile. The thick dashed line is the adiabatic parcel curve. Following Weisman and Klemp (1982).

convective updraft. Because of this dependence, the experiments presented in this paper are designed to most naturally isolate the recirculation mechanism while maintaining full microphysical representation to best simulate deep moist convection as seen in reality. The experiments consist of a control simulation that uses the full two-moment microphysical scheme (Meyers et al. 1997; Saleeby and Cotton 2004) for all hydrometeors (herein referred to as “2MOM”) and three sensitivity simulations that use two-moment microphysics for the nucleating water species (e.g., cloud water, drizzle, and pristine ice) and one-moment microphysics (Walko et al. 1995) for the remaining hydrometeor species (e.g., rain, snow, aggregates, graupel, and hail) in order to control the variation in hail hydrometeor size, while still keeping the sophisticated nucleation scheme in RAMS active and for best comparison to 2MOM.

The sensitivity simulations all use identical hydrometeor distributions for rain, snow, aggregates, and graupel but vary the mean diameter of the hail size distribution. This control on the hail size distribution requires the use of one-moment microphysics, whereby the mass-mixing ratio is prognosed and the number concentrations are diagnosed from the imposed hydrometeor distributions. Increasing the mean diameter of the hail size distribution results in a lower number concentration and intercept parameter. The range of mean hail sizes tested for the sensitivity experiments was chosen based on those seen in

TABLE 1. The microphysical setup for each experiment, where “2” represents the use of two-moment microphysics (prognostic for mass mixing ratio and number concentration) and “1” represents one-moment microphysics (prognostic for mass mixing ratio). The values in parentheses refer to the mean diameter (mm) of the species and are only present when using one-moment microphysics for that species. The italicized cells highlight the sensitivity experiments.

Experiment	Cloud	Drizzle	Rain	Pristine Ice	Snow	Aggregates	Graupel	Hail
CONTROL (2MOM)	2	2	2	2	2	2	2	2
1MM	2	2	1 (3)	2	1 (3)	1 (3)	1 (3)	<i>1 (1)</i>
5MM	2	2	1 (3)	2	1 (3)	1 (3)	1 (3)	<i>1 (5)</i>
1CM	2	2	1 (3)	2	1 (3)	1 (3)	1 (3)	<i>1(10)</i>

the control simulation, which ranged from approximately 0.5 to 5 mm, and are 1 mm (herein referred to as “1MM”), 5 mm (herein referred to as “5MM”), and 1 cm (herein referred to as “1CM”) (Table 1). The variation in hail mean diameter permits some degree of direct control over the recirculation mechanism because as hail size increases, its 1) fall velocity increases, 2) in-cloud residence time decreases, 3) average surface area to volume ratio decreases, and 4) position relative to the convective updraft changes. It should be noted that by simply changing the characteristics of hail hydrometeors, various other microphysical processes will also likely be affected that will lead to changes in squall-line characteristics. This has been shown for supercells (Gilmore et al. 2004; van den Heever and Cotton 2004; Dawson et al. 2010), squall lines (Ferrier et al. 1995; Bryan and Morrison 2012), and bow echoes (Adams-Selin et al. 2013a,b). However, varying the mean diameter of the hail size distribution provides the most direct control over the recirculation mechanism while still representing all of the microphysical processes that are seen in reality, without unintentionally and unknowingly biasing a specific process. To most effectively assess the recirculation mechanism, detailed microphysical analysis for the sensitivity simulations is presented in section 4.

3. Control experiment

a. Squall-line overview

Within the first 10 min of the control simulation (2MOM), deep convection is initiated linearly along the imposed cold pool edge. During the first 3 h (i.e., squall-line spinup), the deep convection organizes into a squall line with typical characteristics. Figure 2 highlights the convective evolution of the 2MOM squall line from hours 2 to 7 after initialization and shows simulated radar reflectivity at a height of 1 km AGL, following the methodology of Matrosov (1999). The zonally propagating squall line is beginning to break down into individual convective cells 2 h into the simulation, as is evident by the 3.5-km-AGL 5 m s⁻¹ updraft contours. Between hours 3 and 7, the squall line transforms into

a mature mesoscale convective system that contains trailing stratiform precipitation and peak reflectivity leading the convective line. Toward the latter half of the simulation, bowing structures develop as RIJs organize within the squall line that are collocated with intense updrafts and heavy precipitation (Figs. 2d–f).

The data in some analyses presented hereafter have been averaged first meridionally relative to the surface cold pool boundary, and then temporally, thus effectively resulting in a vertical cross section of the squall line in order to obtain a cohesive view of the simulated system. The cold pool boundary (or gust front) is defined by the $-0.05 \text{ m}^2 \text{ s}^{-2}$ buoyancy surfaces. Buoyancy is defined after Tompkins (2001) as

$$B \equiv \frac{g(\theta_\rho - \bar{\theta}_\rho)}{\bar{\theta}_\rho}, \quad (1)$$

where $\theta_\rho = \theta(1 + 0.608q_v - q_t)$ is the density potential temperature (Emanuel 1994) and includes the effects of condensate loading (q_v and q_t are the vapor and total condensate mixing ratios), and $\bar{\theta}_\rho$ is the mean density potential temperature downshear of the squall line at the respective y grid point. It should be noted that all quantities presented as averages have been calculated prior to spatial and temporal averaging.

The simulation produces an upshear-tilted squall line, as is obvious from several classic squall-line characteristics evident in Fig. 3. Front-to-rear flow, broad anvil divergence, and a RIJ located 2–4 km AGL are apparent in the storm-relative wind field (Fig. 3a; Weisman 1992, 1993; Trier et al. 1997; Parker and Johnson 2000; Houze 2004). Also, the convective updraft can be seen extending from the cold pool up through the anvil and downshear of the mesoscale downdraft (Fig. 3b; Smull and Houze 1987). The spatial disconnect between the cold pool–forced updraft and the midlevel updraft evident here has been seen in other observational and modeling studies (Jorgensen et al. 1997; Trier et al. 1997; Takemi and Satomura 2000; Bryan et al. 2003, 2007; Xiao and Sun 2007; Fierro et al. 2009; Morrison et al. 2009) and may be explained by the finer-scale grid

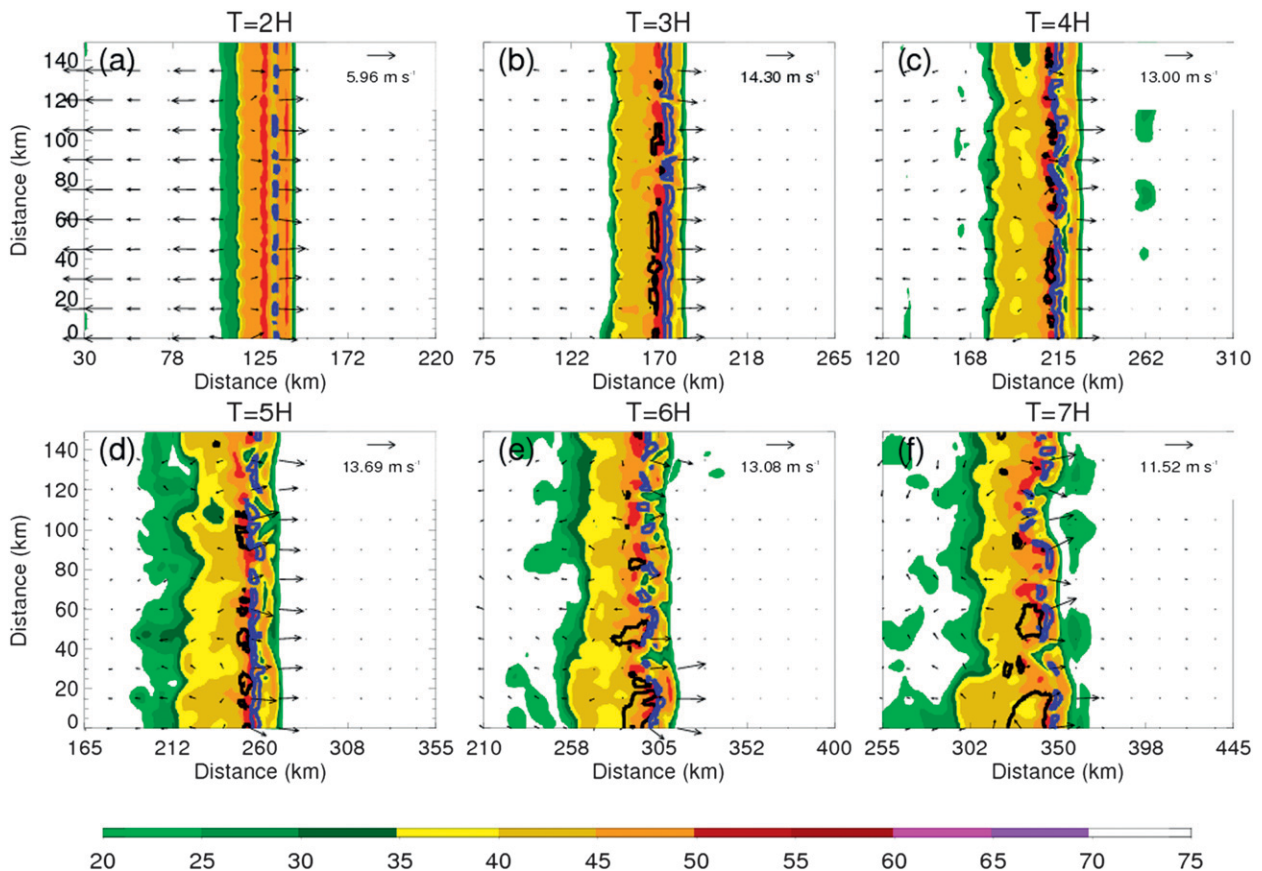


FIG. 2. Simulated base radar reflectivity (dBZ) of 2MOM at 1 km AGL using the methodology of Matrosov (1999) for $T =$ (a) 2, (b) 3, (c) 4, (d) 5, (e) 6, and (f) 7 h into the simulation. The surface winds are shown (vectors) along with the maximum surface wind reference vector in the upper-right corner for each time. Two-sigma standard deviation anomalies of U wind at 3.5 km AGL (black contours) and updraft speeds of 5 m s^{-1} (blue contours) are also shown.

spacing used in these simulations (500 m) compared with the more commonly used 1-km horizontal grid spacing (e.g., Fovell and Tan 1998; WR04) [see Fig. 5b in Bryan et al. (2003) showing simulated squall lines in a strongly sheared environment using varying grid spacings]. The y component of relative vorticity (Fig. 3c) shows the balance between positive and negative vorticity on the downshear and upshear flanks of the updraft, respectively, as described by RKW88 (Tao et al. 1995; Meng et al. 2012). Finally, the pressure perturbation field (Fig. 3d), which has been calculated relative to the mean environmental pressure field ahead of the squall line, shows the rear-to-front horizontal pressure gradient that is hypothesized to partially drive the RIJ (Schmidt and Cotton 1990; Weisman 1992; Grim et al. 2009). The generation of the peak midlevel updraft velocity (and associated local minimum in perturbation pressure) just below the freezing level is the primary focus of this study and will be further discussed in the next section.

b. Recirculation mechanism

The upshear-sloped squall line presented in this paper contains a midlevel circulation centered at the freezing level on the upshear side of the main updraft. This circulation is found to enhance the midlevel updraft of the simulated squall line and it stems from the incorporation of RIJ-transported hydrometeors into the midlevel convective updraft. Figure 4 shows the cold pool and temporally averaged microphysical processes contributing to the recirculation mechanism that help to invigorate the midlevel updraft. The recirculation mechanism begins with hail that has been ejected upshear from the main convective updraft owing to the front-to-rear (FTR) flow above the freezing level (Fig. 3a). The hail hydrometeors have grown large enough to descend below the freezing level and into the RIJ. They are then advected downshear toward the updraft, where they become entrained back into the updraft (Fig. 4a). The other ice species (pristine ice, snow, aggregates, and graupel) all

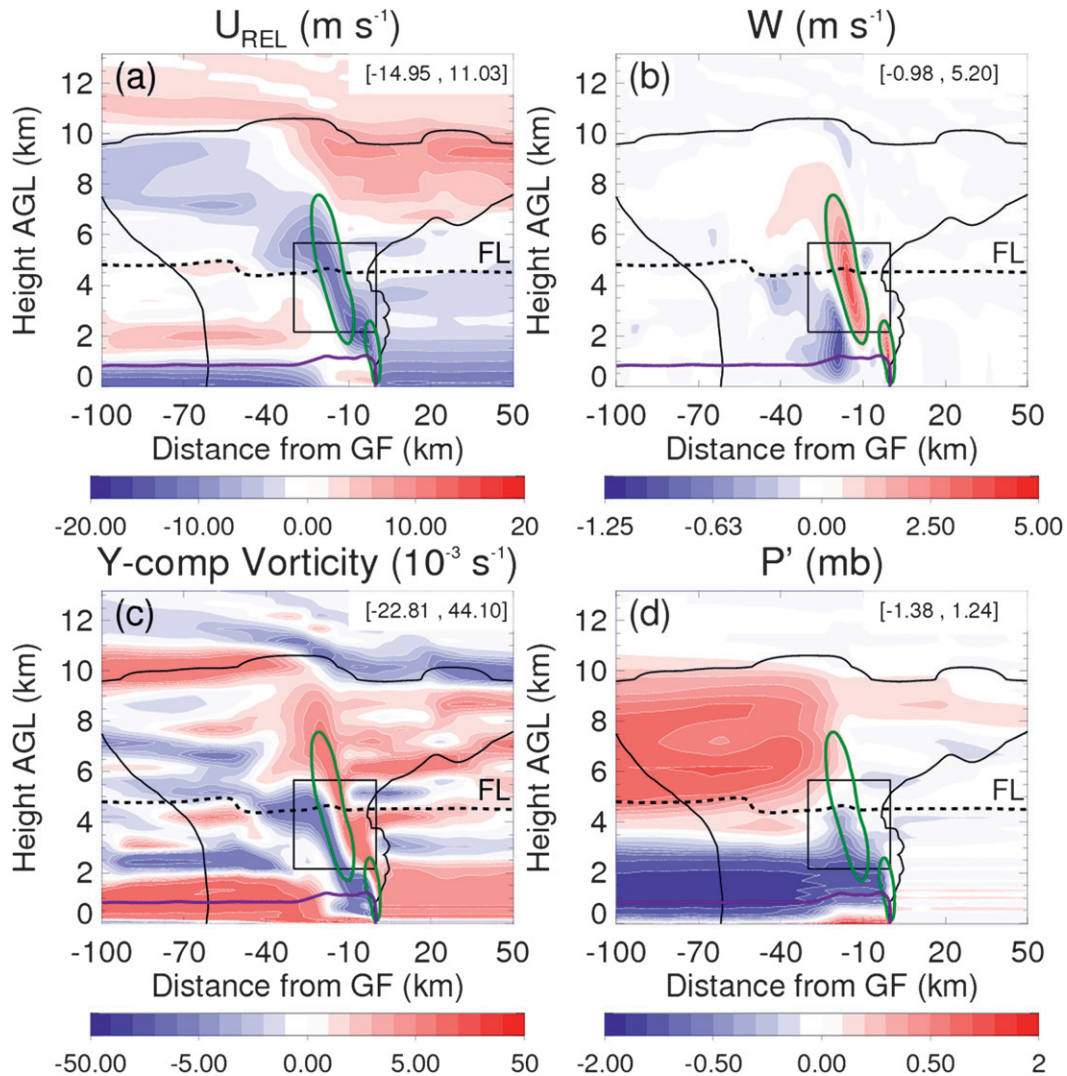


FIG. 3. Control squall line from simulation hours 3–7 that has been temporally and meridionally averaged along the gust front. Each vertical cross section is expressed as a horizontal distance from the gust front (x axis) and a vertical distance AGL (y axis). Shown on each cross section is the squall-line cloud boundary (thick black line; 0.05 g kg^{-1} total condensate), the freezing line (dashed black line), the cold pool boundary [thick purple line; $-0.05 \text{ m}^2 \text{ s}^{-2}$ following Tompkins (2001)], the 1 m s^{-1} updraft region (thick green line), a box centered over the midlevel updraft that is the domain shown in Fig. 4, and [min, max] values for the shaded quantities of (a) system-relative U -component wind (m s^{-1}), (b) vertical velocity (m s^{-1}), (c) y -component relative vorticity (10^{-3} s^{-1}), and (d) pressure perturbation (hPa).

have densities and associated fall speeds that are too low to allow sedimentation into the RIJ sufficiently close to the updraft in order to become entrained. Herein, entrainment is defined as the incorporation of air or hydrometeors into the main convective updraft that originated from external regions. Because the hail advection by the RIJ is occurring below the freezing level, partial melting of the hailstones (Fig. 4b) leads to shedding of liquid water, which generates rain hydrometeors (Fig. 4c) that are also advected by the RIJ into the updraft. The extra hail and rain hydrometeors within the

updraft, which contains supersaturated air, increases the net surface area onto which vapor can be deposited and thus enhances the hydrometeor growth process of vapor deposition (Fig. 4d). This more effectively removes supersaturation (Fig. 4e) and positively contributes to the latent heating within the convective updraft. This can be seen in the vicinity of the marker in Fig. 4 by the minimum in supersaturation (Fig. 4e) collocated with the positive hail flux (Fig. 4a) and a local maximum in rain mixing ratio (Fig. 4c).

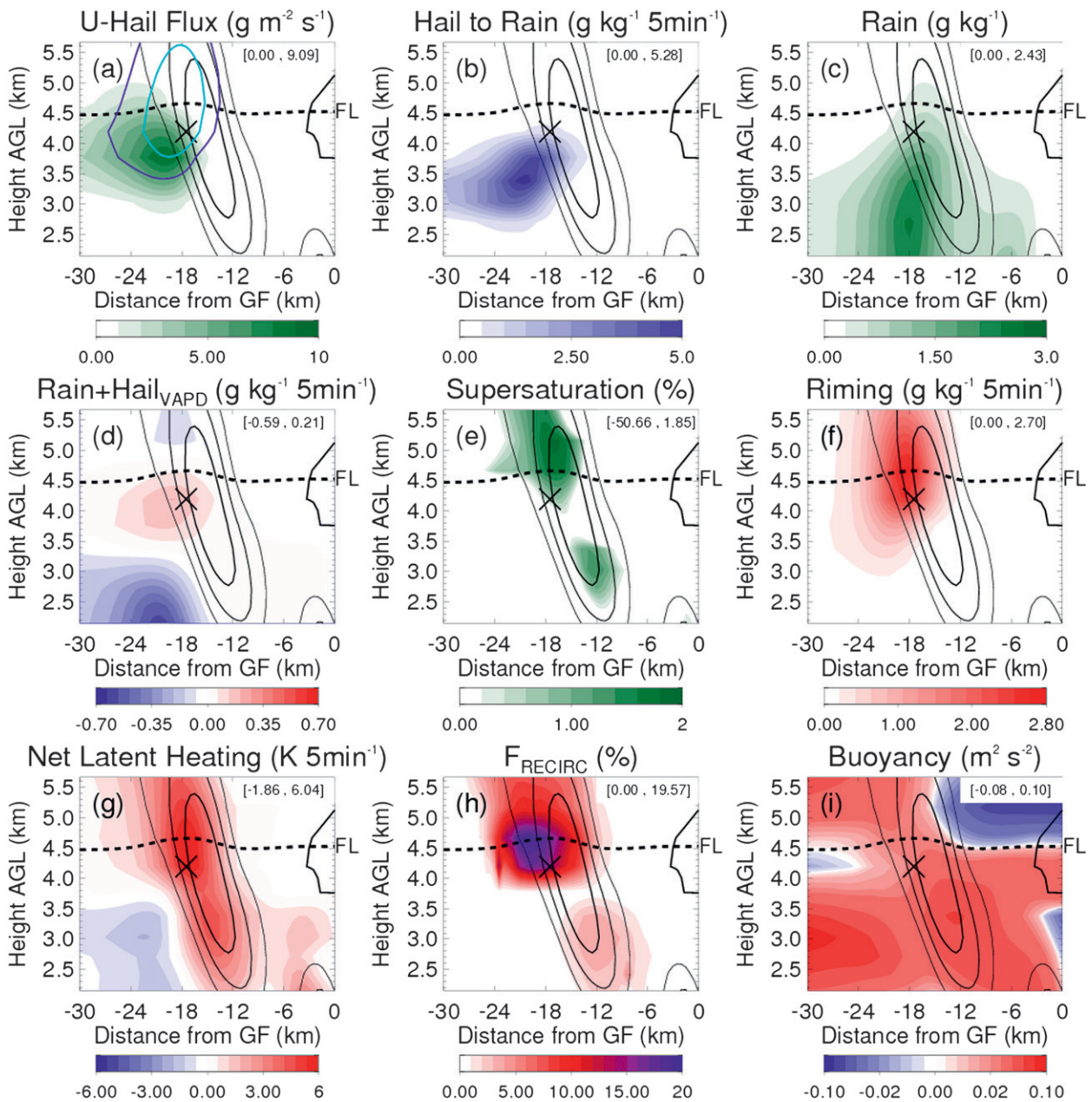


FIG. 4. As in Fig. 3, except the domain shown is centered over the recirculation mechanism and can be seen relative to the entire squall line as the box in Fig. 3. The cross near the center of each figure is for a point of reference between the figures. The black lines in the center of each image are the 1, 2, and 3 m s^{-1} updraft contours, the dashed line is the freezing level, the thick black contour at the right edge of each image is cloud boundary, and the shaded contours are (a) positive zonal flux of hail condensate ($\text{g m}^{-2} \text{ s}^{-1}$) with hail mixing ratios contoured [0.5 (dark blue) and 1.0 (light blue) g kg^{-1}], (b) ice-to-rain conversion mixing ratio averaged as 5-min differences [$\text{g kg}^{-1} (5 \text{ min})^{-1}$], (c) rain mixing ratio (g kg^{-1}), (d) vapor deposition onto hail and rain hydrometeors expressed as a mixing ratio averaged over 5-min differences [$\text{g kg}^{-1} (5 \text{ min})^{-1}$], (e) supersaturation (%), (f) total riming expressed as a mixing ratio averaged as 5-min differences [$\text{g kg}^{-1} (5 \text{ min})^{-1}$], (g) total latent heating minus total latent cooling [$\text{K} (5 \text{ min})^{-1}$], (h) net latent heating due to the recirculation mechanism [Eq. (2)], and (i) buoyancy ($\text{m}^2 \text{ s}^{-2}$).

The hailstones that are entrained into the midlevel convective updraft may collide with cloud and rain droplets already in the updraft. Providing that the internal energy of the hailstones is sufficiently low [i.e., the

hailstones are cold; see Walko et al. (1995) for a detailed description of the treatment of the internal energy of hail within RAMS], the hailstones can then become rimed by cloud droplets and rain hydrometeors (Fig. 4f).

This process also contributes positively to the latent heating within the convective updraft. Furthermore, some of the RIJ-advected rain hydrometeors within the updraft that have not yet collided with hailstones can also be transported higher into the storm and later serve as a source of latent heat from fusion. This will be discussed further later in this section.

To assess the relative importance of the recirculation mechanism that has just been described, a recirculation heating fraction is used that includes all of the latent heating processes directly involved in the mechanism relative to the total latent heating. The total latent heating of the midlevel updraft region is shown in Fig. 4g and includes the processes of condensation, evaporation, ice deposition, ice sublimation, riming, melting, cloud nucleation, and ice crystal nucleation. The microphysical processes that are not directly associated with the recirculation mechanism are cloud droplet growth, cloud droplet nucleation, drizzle growth, drizzle nucleation, and the processes associated with pristine ice, snow, aggregates, and graupel; they may however be indirectly related through feedbacks in updraft strength and supersaturation. The fraction of latent heating due to those microphysical processes directly associated with the recirculation mechanism can then be defined as

$$F_{\text{RECIRC}} = \frac{\dot{Q}_{\text{NET}} - \dot{Q}_{\text{NONRECIRC}}}{\dot{Q}_{\text{NET}}}, \quad (2)$$

where F_{RECIRC} is the recirculation heating fraction, \dot{Q}_{NET} is the total latent heating from all microphysical processes, and $\dot{Q}_{\text{NONRECIRC}}$ is the net latent heating not associated with the recirculation mechanism (i.e., cloud droplet growth, cloud droplet nucleation, drizzle growth, drizzle nucleation, pristine ice, snow, aggregates, and graupel). As can be seen from Eq. (2), F_{RECIRC} becomes larger as the processes not associated with the recirculation mechanism become less important, or as the processes associated with rain and hail become more important. It can also be seen from Eq. (2) that 1) if \dot{Q}_{NET} becomes small, then slight variations in cloud latent heating relative to the net latent heating can lead to relatively large values of F_{RECIRC} , and 2) if $\dot{Q}_{\text{NONRECIRC}}$ is more negative than \dot{Q}_{NET} then false positive values of F_{RECIRC} can exist. The recirculation heating fraction is shown in Fig. 4h, but has been truncated to where the mean updraft speed is greater than 0.5 m s^{-1} and values of \dot{Q}_{NET} and $\dot{Q}_{\text{NONRECIRC}}$ are both positive in order to isolate the recirculation mechanism and to remove the caveats of the calculation just described. It is clear that F_{RECIRC} is maximized in the region of the updraft close to and just below the freezing level (Fig. 4h), which is collocated with the entraining hail (Fig. 4a) and rain (Figs. 4b,c)

hydrometeors and the microphysical processes associated with the recirculation mechanism (Figs. 4a–f). It should be noted that because it is difficult to estimate the fraction of hydrometeors that are recirculated, F_{RECIRC} is applied to all hydrometeors and represents an instantaneous, maximum possible estimate. However, indirect feedbacks on the squall line that are not included in F_{RECIRC} may also occur.

It is likely that in addition to the entrainment of hail into the updraft, less-buoyant nonupdraft air is also being mixed into the updraft that can counteract the positive contribution of latent heating by the recirculation mechanism. Figure 4i shows the mean buoyancy distribution in and around the midlevel updraft and includes the effects of condensate loading. From the buoyancy field it can be seen that the peak in positive buoyancy occurs toward the lower portion of the main updraft, centered around 3.5 km AGL, which is due to condensational growth of both cloud and rainwater. As rain condensational growth is included in \dot{Q}_{NET} , this peak in positive buoyancy shows up in the F_{RECIRC} field (Fig. 4h); however, its value is small. Moving higher up in the updraft it can be seen that the region of largest positive buoyancy is shifted toward the upshear side of the updraft (Fig. 4i) and matches well with the location of maximum F_{RECIRC} (Fig. 4h). This suggests that the microphysical processes associated with the recirculation mechanism contribute positively to the net buoyancy field in the midlevel updraft.

To see how this mechanism operates for an individual convective cell, Fig. 5 shows a vertical cross section through a well-organized portion of the squall line (Fig. 5a) 7 h into the simulation. From this cross section, the following processes (Fig. 5b) can be seen that lead to an enhancement in F_{RECIRC} (Fig. 5c): 1) hail is falling into the RIJ from above the freezing level, 2) the falling hail has net condensational growth below the freezing level both within the RIJ and in the upshear flank of the updraft, 3) the melting hail generates rain hydrometeors in the updraft and within the RIJ that are then fluxed into the updraft at approximately 3–3.5 km AGL, and 4) because of their slower fall velocity, some of the ingested raindrops can be transported higher in the updraft (i.e., recirculated) to then serve as a source of latent heat by freezing onto hailstones. These processes generate local F_{RECIRC} values up to approximately 30% (Fig. 5c); however, positive feedbacks can also potentially invigorate the squall line even more than suggested by this value, and will be assessed in section 4.

It is obvious that ice processes will become more important in generating net positive latent heating at and above the freezing level (Fig. 4h) for squall lines; however, it is not obvious that ice processes below the freezing

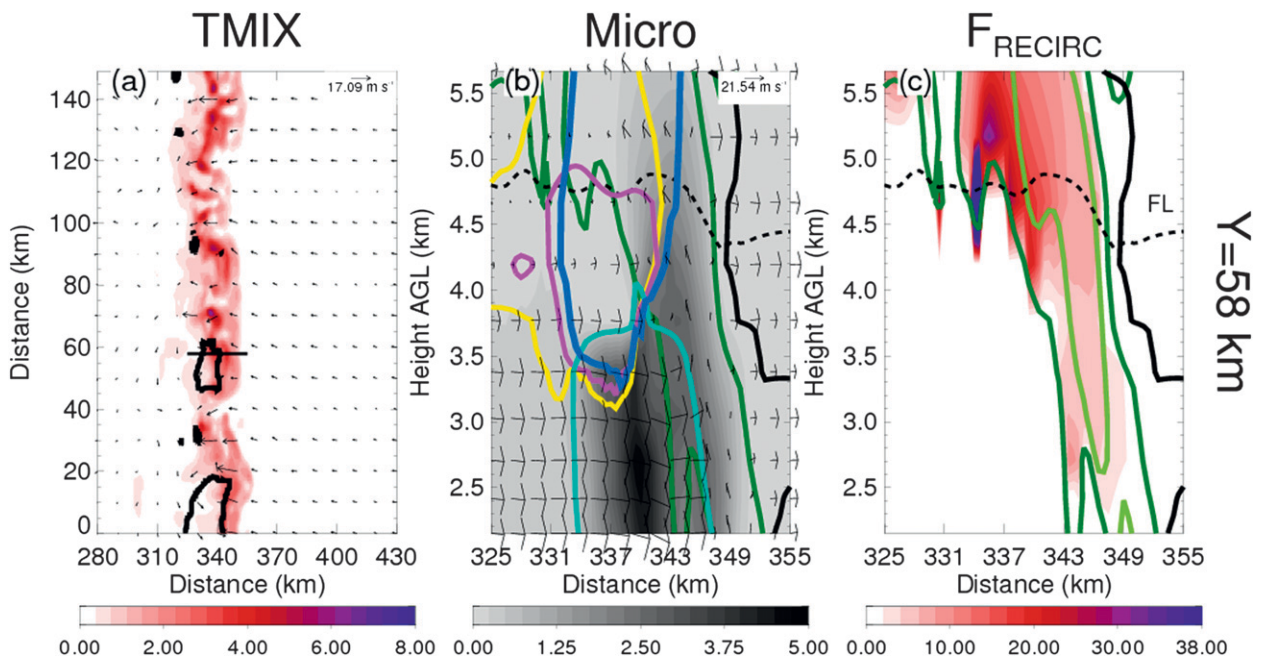


FIG. 5. (a) Plan-view cross section of total condensate (shaded) and (b),(c) vertical cross sections through an organized segment of the squall line at $y = 58$ km. The location of the vertical cross section is depicted by the black horizontal line in (a). In (b) rain mixing ratio (g kg^{-1} ; shaded), hail mixing ratio (0.5 g kg^{-1} ; blue contour), riming of rain by hail [$0.5 \text{ g kg}^{-1} (5 \text{ min})^{-1}$; yellow contour], net vapor deposition of hail [$0.05 \text{ g kg}^{-1} (5 \text{ min})^{-1}$; magenta contour], horizontal rain flux ($0.05 \text{ g m}^{-2} \text{ s}^{-1}$; light blue contour), U - W wind vectors, 1 m s^{-1} vertical velocity (dark green contour), the freezing level (dashed), and cloud boundary (thick black) are shown. In (c) the recirculation heating fraction (shaded), 1 m s^{-1} (dark green contour) and 5 m s^{-1} (light green contour) vertical velocity, freezing level (dashed), and cloud boundary (thick black) are shown.

level can assist in strengthening the updraft through a positive contribution to latent heating (Fig. 4h) that enhances buoyancy (Fig. 4i) and potentially induces a positive feedback on squall-line strength. This is the fundamental role of the recirculation mechanism, which is summarized in schematic form in Fig. 6, and will be further analyzed in the next section through sensitivity experiments.

4. Sensitivity experiments

Assessing the precise contribution of the recirculation mechanism to the intensity of a simulated squall line is not simple, as it has been shown that microphysics and dynamics within squall lines are intimately connected (e.g., Fovell and Ogura 1988; Ferrier et al. 1995; Adams-Selin et al. 2013a,b; Bryan and Morrison 2012). Systematically turning off processes involved in the recirculation mechanism (e.g., hail riming or vapor deposition onto hail) within the microphysics scheme in order to assess their individual importance does not necessarily isolate cause and effect because of the often nonlinear responses within many microphysical-dynamical pathways. For example, when simulating a hailstorm that occurred over Germany, Noppel et al. (2010) ran sensitivity simulations

that varied the concentration of CCN and the shape of the cloud drop distribution and concluded that the strong coupling between numerous microphysical processes “makes it difficult to foresee, what will happen, when one microphysical parameter is changed” (p. 286). In an effort to better understand the microphysical-dynamical pathways in a supercell storm, Morrison (2012) performed an ensemble of simulations in which various

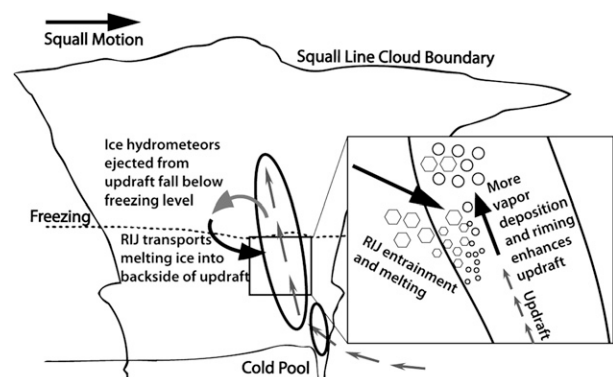


FIG. 6. Idealized schematic showing the microphysical mechanism aiding enhancement of the midlevel updraft of a squall line. A view of the processes occurring near the freezing level is shown within the box in the right half of the schematic.

microphysical processes are turned off and found a “network-like” response for the supercell in which other microphysical processes act to compensate for the excluded process.

To isolate the importance of the recirculation mechanism while still preserving all of the microphysical processes and not unintentionally biasing specific processes, a sensitivity experiment has been designed that varies the mean diameter of the hail hydrometeor distribution. It was shown in the previous section that the recirculation mechanism stems from the entrainment of hail and rain hydrometeors into the midlevel updraft of a squall line. By altering the size characteristics of hail that will result in changes to both hail and rain microphysics and the position of hail sedimentation relative to the RIJ and midlevel updraft, the recirculation mechanism’s importance on squall lines can potentially be assessed. The four experiments that accomplish this task will be presented in this section, and consist of the control simulation (2MOM; see section 3) and three sensitivity simulations that vary the mean diameter of the hail size distribution among 1 mm (1MM), 5 mm (5MM), and 1 cm (1CM).

a. Squall-line characteristics

To highlight some characteristic differences and similarities between the four squall lines, Fig. 7 shows the 1-km-AGL simulated reflectivity at three times during the simulations that span the first 4 h of the analysis period. For each simulation, it is evident that bowing in the reflectivity field is collocated with strong updraft and anomalously strong RTF flow in the midlevels, which persists for multiple hours. This indicates that each squall line is well organized (Weisman 1992, 1993) and freely evolving. Relative to the control simulation (2MOM), it can be seen that 1) squall-line propagation is very similar for all simulations, 2) the 1MM simulation shows the most expansive stratiform region and qualitatively looks the most similar to 2MOM, 3) bowing structures are evident for all simulations, and 4) the highest reflectivity occurs with the 1CM simulation, which is due to more large hail reaching the surface, as reflectivity is strongly dependent on hydrometeor size. From Fig. 7 it is clear that by simply changing the mean diameter of hail, notable structural differences occur. These differences could be influenced by changes to the cold pool, which alters the dynamics of the squall line according to RKW88, and has also been linked to microphysics by other studies such as Luo et al. (2010), Adams-Selin et al. (2013a,b), and Bryan and Morrison (2012). Therefore, in order to assess the significance of the recirculation mechanism on the intensity of the simulated squall lines, the influence of the cold pool for each squall

line will be investigated through the application of RKW theory. This will help to isolate the impacts of the cold pool from the recirculation mechanism for the squall lines.

Given that the base state shear profile is not varied between simulations, the cold pool propagation speed dominates the $C/\Delta U$ variability among the simulations. Traditionally, a theoretical measure of C is used based on density current theory (e.g., RKW88; WR04; Bryan et al. 2006) and is given by (Benjamin 1968)

$$C_B^2 = 2 \int_0^H (-B) dz, \quad (3)$$

where C_B represents the cold pool propagation speed based on the theoretical buoyancy calculation, B represents the buoyancy defined in Eq. (1), and H represents the height of the cold pool, which has been defined for every meridional point by the zonal point (often about 5 km behind the gust front) that has the greatest continuous depth of cold pool buoyancy ($-0.05 \text{ m}^2 \text{ s}^{-2}$). Most previous studies also all make use a free-slip bottom boundary condition that allows C_B for squall lines to behave similarly to classical density current theory (e.g., RKW88; WR04; Bryan et al. 2006). However, in reality the lower boundary is not a free-slip surface and neither are the simulations performed here. As such, C_B will be compared to a direct measure of squall-line propagation that is calculated by tracking the location of the gust front in time (C_D). This calculation most precisely describes the motion of the squall line while including the effects of surface friction, which is implicit for squall lines in reality.

The comparison between C_D and C_B and their respective $C/\Delta U$ values are shown in Table 2 as time and meridional averages. The most obvious difference between C_D and C_B is that C_B is 50%–60% larger than C_D , which is primarily due to the inclusion of surface drag because the mean wind should act to increase the ground-relative cold pool propagation speed (Moncrieff and Liu 1999; Corfidi 2003). The values of C_B ($\sim 15\text{--}20 \text{ m s}^{-1}$ for instantaneous speeds) match well with those in other studies using the Weisman–Klemp sounding (e.g., WR04; Bryan et al. 2006). In WR04’s revisit of RKW88, they showed that when using three-dimensional simulations and calculating ΔU over the lowest 2.5 km AGL, squall-line intensity is maximized when $C_B/\Delta U \sim 1.0\text{--}1.7$ (see Table 1c in WR04). From Table 2, it can be seen that the $C_B/\Delta U$ values for the experiments here, which also have the shear within the lowest 2.5 km AGL, fall within this range. However when using $C_D/\Delta U$, the ratios are lower and range from 0.7 to 1.3, which is not surprising given that surface drag is included in the simulations. In

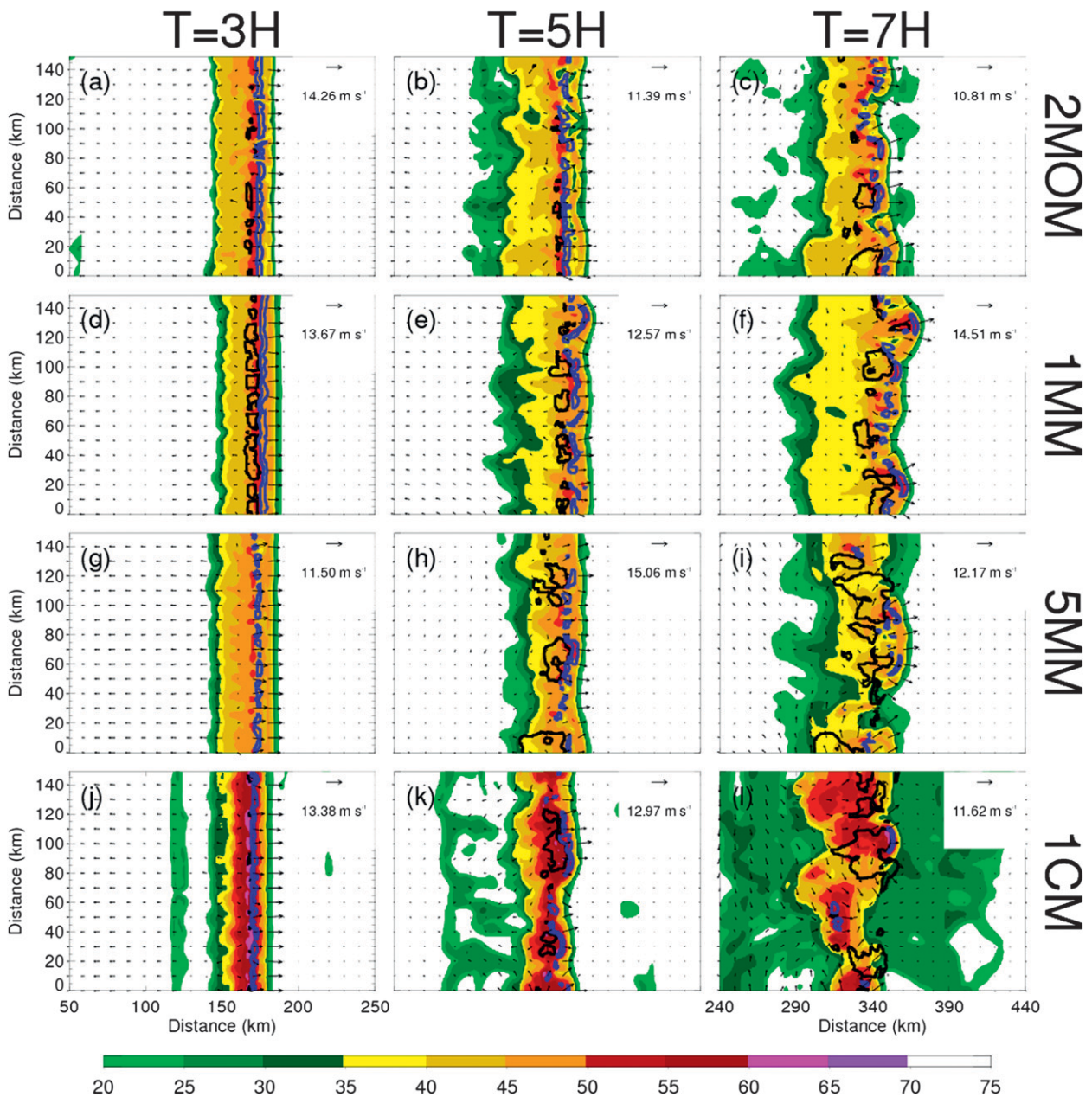


FIG. 7. Simulated base radar reflectivity (dBZ; Matrosov 1999) of (a)–(c) 2MOM, (d)–(f) 1MM, (g)–(i) 5MM, and (j)–(l) 1CM at 1 km AGL for $T =$ (left) 3, (middle) 5, and (right) 7 h into the simulation. The surface winds (vectors) are shown along with the maximum surface wind reference vector in the upper-right corner for each image. Two-sigma standard deviation anomalies of U wind at 3.5 km AGL (black contours) and updraft speeds of 5 m s^{-1} (blue contours) are also shown.

both sets of C calculations, a modest decrease in cold pool speeds is evident as hail size increases (Fig. 9), which has also been noted by other numerical studies (Szeto and Cho 1994; van den Heever and Cotton 2004; Adams-Selin et al. 2013a,b). While a trend is evident in cold pool speeds, the $C/\Delta U$ ratios are largely similar between simulations and centered within the range where each squall line should be close to its maximum

system intensity. For all subsequent analysis, C_D will be used as the metric for cold pool propagation speed.

Based on RKW theory, the analysis above demonstrates that all these squall lines should be near their maximum system intensity; however, changes in cold pool intensity has been shown to lead to changes in squall-line organization (Szeto and Cho 1994; Adams-Selin et al. 2013b). Figure 8 shows vertical cross sections

TABLE 2. Temporal and meridional average values of C_B , C_D , $C_B/\Delta U$, and $C_D/\Delta U$ between hours 3 and 7 for each simulation.

Experiment	C_B	C_D	$C_B/\Delta U$	$C_D/\Delta U$
CONTROL (2MOM)	18.36	11.35	1.47	0.91
1MM	18.73	11.95	1.50	0.96
5MM	17.61	11.48	1.41	0.92
1CM	16.31	11.09	1.30	0.89

of the basic fields of system-relative U wind (relative to C_D), vertical velocity, and pressure perturbation (calculated relative to the presquall environment) for all experiments, which have been averaged meridionally with respect to the gust front and temporally. As hail size decreases, the FTR flow strengthens and the RIJ extends closer to the front of the storm near the midlevel updraft (cf. Figs. 8d,g,h). The vertical velocity field also shows similar trends in that as hail size decreases, the midlevel updraft increases and the mesoscale downdraft strengthens (cf. Figs. 8e,h,k). Upon comparing simulations of a bow echo in which characteristics of graupel were changed to represent hail, similar trends were seen by Adams-Selin et al. (2013b), whereby as the hydrometeors were more graupel-like the bow echo contained stronger updrafts and faster RTF flow. The squall lines of 2MOM and 1MM are the only simulations that have a significant minimum in pressure owing to latent heating within the main convective updraft near the freezing level, further indicating that they are the most organized of the group.

As WR04 note, the “optimal” state of squall lines is not clear cut, as many parameters can define system intensity. Mean precipitation rate (Fig. 9a) generally decreases with increasing hail size, and the 1MM and 2MOM produce the most amount of precipitation. Similar trends are seen for total water path (TWP; Fig. 9b), except the 2MOM squall line has less TWP than all squall lines from time $T = 3$ to 4.5 h, but still follows the temporal trend of 1MM closely. The time series of meridionally averaged C_D and $C_D/\Delta U$ are shown in Fig. 9c. The sensitivity simulations all show a relatively steady mean cold pool speed and associated $C_D/\Delta U$ close to 1; however, the 1CM cold pool is consistently slower than the 1MM cold pool by about 10%, and the 5MM cold pool is variable. This indicates that the squall lines are all stable and near their maximum system intensity according to RKW88, but the 1MM cold pool is indeed stronger.

To better understand how the structure of the squall lines differs between simulations, Fig. 10 shows horizontally and temporally averaged vertical profiles of various quantities that assess squall-line organization and intensity. The line-perpendicular wind (Fig. 10a) shows an enhancement of both the RIJ (the local maxima in U

at about 2 km AGL) and the FTR flow (the local minimum in U at about 6 km AGL) with decreasing hail size, signifying that as hail decreases, the convective momentum transport is more pronounced (Lane and Moncrieff 2010). A smooth trend in vertical velocity is also seen (Fig. 10b), whereby as hail size decreases the domain-averaged vertical velocity increases systematically through the depth of the troposphere. A similar trend is also evident in total condensate (Fig. 10c); however, the 2MOM squall line contains smaller amounts of condensate above the freezing level. Throughout most of the troposphere, buoyancy shows little variation between simulations (Fig. 10d), except near 1) the freezing level where buoyancy increases with decreasing hail size, and 2) the surface where a slight decrease in buoyancy is evident with smaller hail size, supporting the cold pool trend previously discussed (Table 2 and Fig. 9c). These trends highlight the importance of the ice phase for squall-line intensity and organization, which will be discussed in the next subsection via the recirculation mechanism.

As hail size decreases, the total upward mass flux (MF) increases systematically throughout the troposphere (Fig. 10e). Additionally, when the updrafts are sampled for deep convection where $W > 1 \text{ m s}^{-1}$ (Fig. 10f) and $W > 2 \text{ m s}^{-1}$ (Fig. 10g), the trend also holds, indicating that convective MF increases with decreasing hail size. Similarly, the mesoscale convective downdrafts are enhanced as hail size decreases (Fig. 10h), highlighting the importance of ice microphysics in overall squall-line organization. To assess the intensity of the squall line as a whole, the fraction of the domain that satisfied the sampling conditions for updrafts and downdrafts are plotted below their corresponding figure (Figs. 10i–l). With the exception of $W > 0 \text{ m s}^{-1}$ (Fig. 10i), which shows virtually no trend, all updraft and downdraft conditions show a large (up to a factor of about 2) increase in domain coverage with decreasing mean hail size. The trends in both greater total mass flux (Figs. 10e–g) and increased domain coverage (Figs. 10i–k) as hail size decreases indicates consistency regardless of the sampling condition applied. The same trends are seen with the strength of the downdrafts increasing with decreasing hail size (Figs. 10h,l).

The latent heating profiles can provide insight into the trends seen in the vertical mass flux (Figs. 10m–o). The most significant changes in the net latent heating for the sensitivity experiments occur in the mixed-phase region (Fig. 10m), where the sensitivity to hail size is most profound. As hail size decreases, the net latent heating increases. This is likely the cause of the increase in buoyancy for smaller hail sizes (Fig. 10d), as the environmental conditions have been held fixed between simulations and increased hydrometeor loading has been found to increase

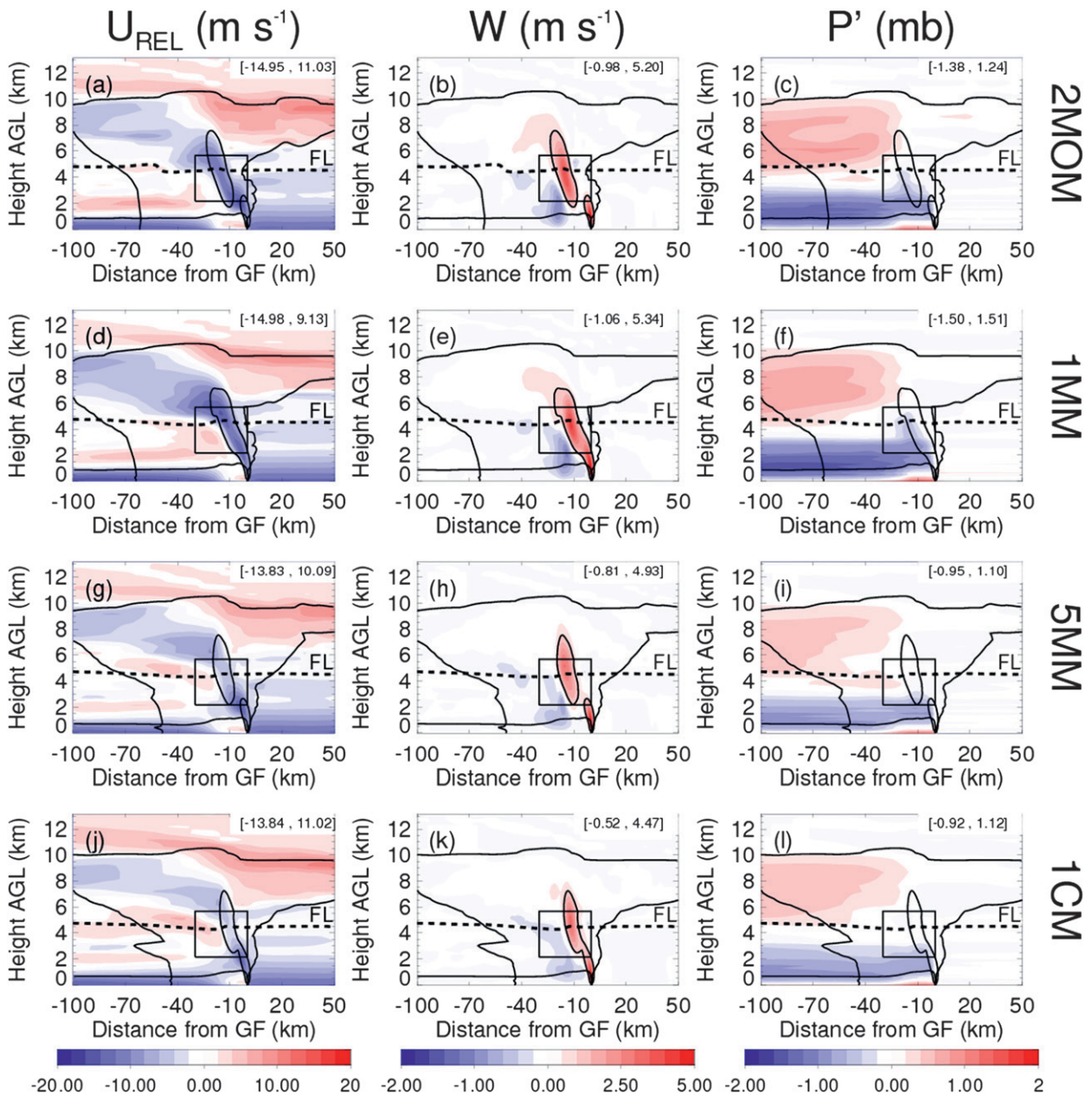


FIG. 8. Gust front and temporally averaged for (a)–(c) 2MOM, (d)–(f) 1MM, (g)–(i) 5MM, and (j)–(l) 1CM squall line from simulation hours 3–7. Each vertical cross section is expressed as a horizontal distance from the gust front and a vertical distance AGL. Shown on each cross section is the squall-line cloud boundary (thick black line; 0.05 kg^{-1} total condensate), the freezing line (dashed black line), the cold pool boundary [(thin black line; $-0.05 \text{ m}^2 \text{ s}^{-2}$ following Tompkins (2001)], the 1 m s^{-1} updraft region (thin black line), a box centered over the midlevel updraft that is the domain shown in Fig. 12, and [min, max] values for the shaded quantities of (left) system-relative U -component wind (m s^{-1}), (middle) vertical velocity (m s^{-1}), and (right) pressure perturbation (hPa).

with decreasing hail size, which actually counteracts this trend. Separating net latent heating into its phase components, the latent heat of fusion helps to explain the signature seen in convective downdrafts (Figs. 11h,l), where increased melting occurs with smaller hail sizes, thus leading to more negative buoyancy (Fig. 10n). This is not

surprising given the increase in surface area associated with smaller hail hydrometeors, which is the largest factor in melting (van den Heever and Cotton 2004). The latent heat of vaporization (Fig. 10o) is predominantly responsible for the trend seen in total latent heating and also shows that above 2 km AGL net condensation increases with

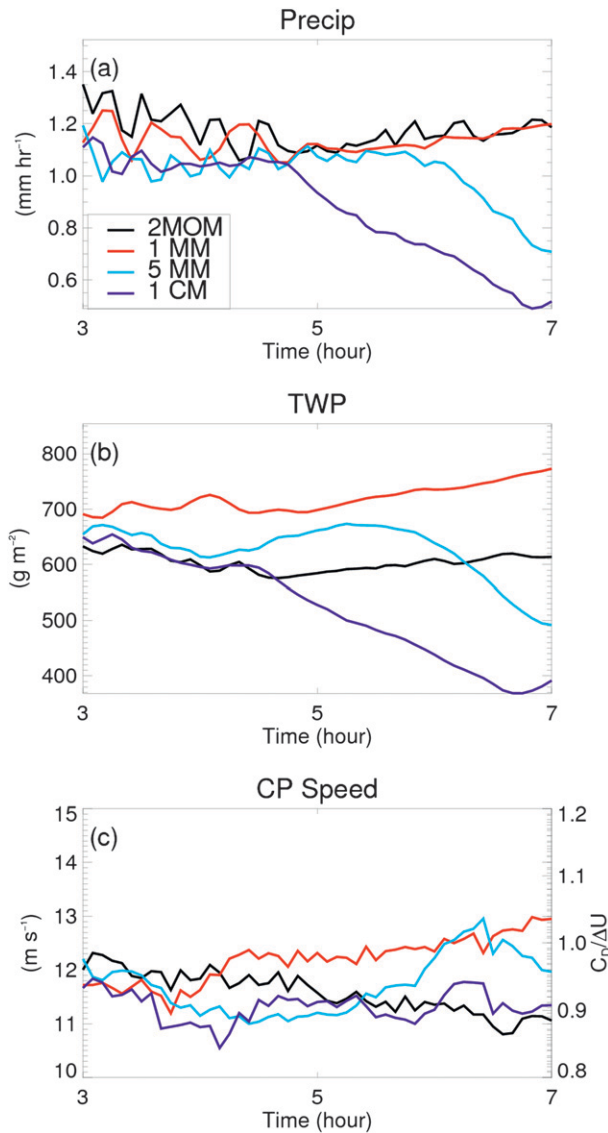


FIG. 9. The time evolution of horizontally averaged plots of (a) surface precipitation, (b) total water path, and (c) cold pool speed with its corresponding $C_D/\Delta U$ values. The legend indicates the respective simulations of 2MOM, 1MM, 5MM, and 1CM.

decreasing hail size, predominantly near the freezing level. Increased evaporation near the surface is also evident as hail size decreases, which contributes to the increase in cold pool speeds.

The analysis in this subsection demonstrates that as the mean hail size decreases, the cold pool speed increases by about 10%. While the variation in cold pool speed is modest between simulations, the trends seen in various assessments of squall-line intensity are more substantial. These trends match well with those seen in microphysical processes near the freezing level that are contributing to increased buoyancy, resulting in stronger

squall lines with decreasing hail size. Because consistent trends in both the cold pools and microphysical processes near the freezing level are occurring, a positive feedback may be assisting squall-line intensity. This feedback can be synthesized whereby ice processes (i.e., the recirculation mechanism) are aiding midlevel updraft invigoration that ultimately leads to more precipitation and to stronger downdrafts. This then leads to stronger cold pools, which enhance low-level convective updrafts and provide more supersaturation for hydrometeor growth, thereby providing more latent energy for the recirculation mechanism. It is important to note that this feedback mechanism may not assist squall-line strength if the system is cold pool dominated (i.e., $C/\Delta U \gg 1$); however, that is not the case here. This will now be examined in more detail via the recirculation mechanism.

b. Recirculation mechanism

To illustrate the differences in the recirculation mechanism as hail size is varied, Fig. 11 shows a single vertical cross section of the microphysical processes and latent heating associated with the recirculation mechanism through the location of the maximum midlevel condensate mixing ratio for each simulation (Figs. 11a,d,g,j). As hail size increases, multiple trends can be seen in Figs. 11e,h,k, including 1) the amount of hail residing in the updraft decreases, 2) the amount of net condensational growth of hail decreases, and 3) horizontal rain flux by the RIJ into the updraft, which serves as an additional source of latent heating by riming as the rain is lofted toward and above the freezing level by the updraft, decreases. These processes all contribute (though not entirely) to the increase in F_{RECIRC} near the freezing level as hail size decreases (Figs. 11f,i,l). Additionally, as hail size increases, the midlevel updraft narrows (Figs. 11f,i,l), which corresponds well with the trends seen in domain updraft coverage (Fig. 10). The narrowing of the convective updraft is not due to condensate loading as there is a consistent trend of increasing hail and rain mass with smaller hail size (Figs. 11e,h,k). These trends all combine to show that the recirculation mechanism is helping to increase the net latent heating that partially drives the midlevel dynamics of the squall line.

By averaging each simulation both meridionally along the gust front and temporally, Fig. 12 shows a comprehensive assessment of the recirculation mechanism and how it becomes more important with decreasing hail size. Following similar logic as with the control experiment (2MOM; section 3b), as hail size decreases (Fig. 12) 1) more hail and rain is fluxed into the midlevel updraft, 2) net condensation onto rain and hail increases below the freezing level, 3) net riming onto hail increases near the freezing level, and 4) F_{RECIRC} increases

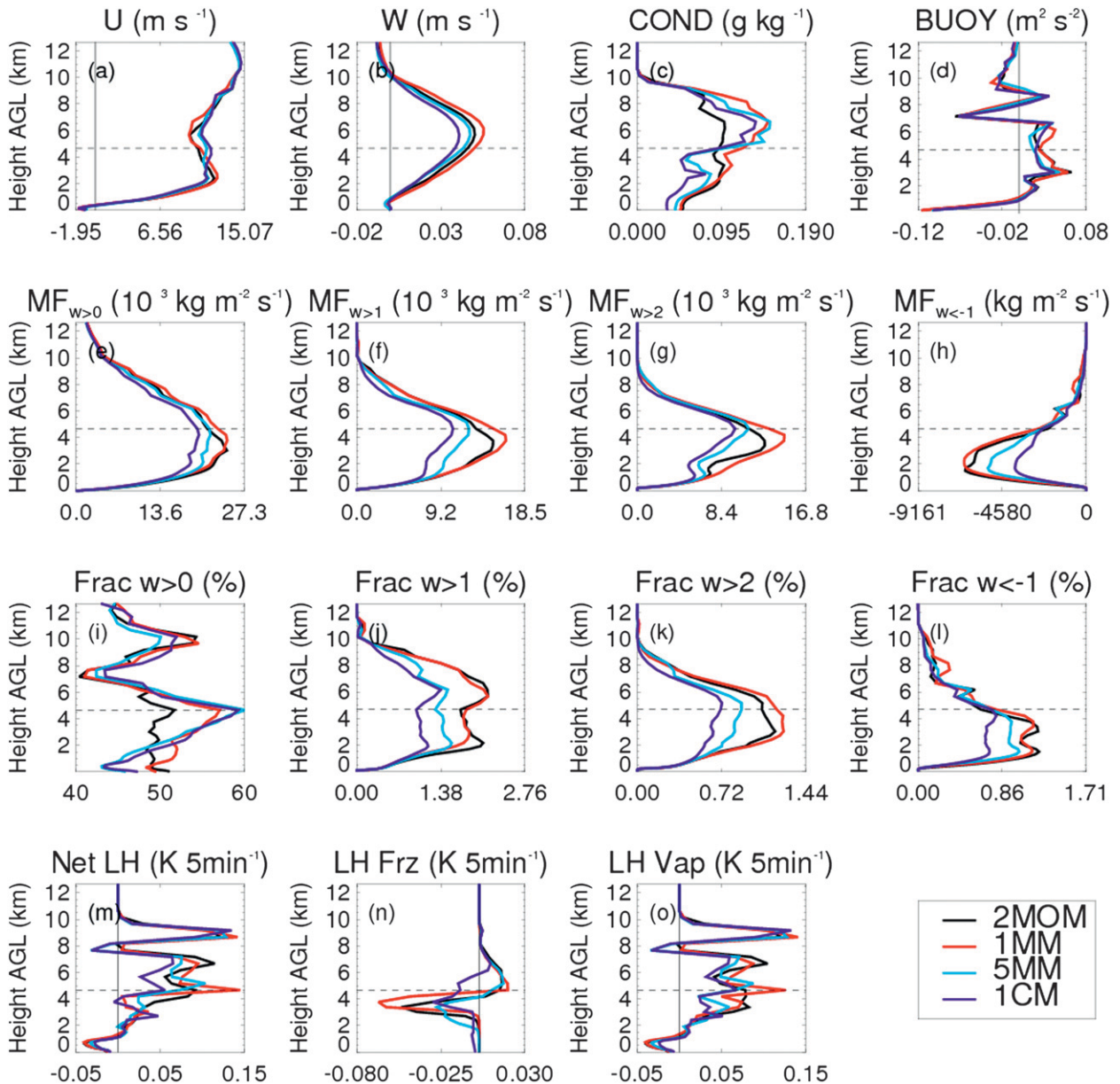


FIG. 10. Horizontally averaged and temporally averaged (between hours 3 and 7) vertical profiles of (a) U wind, (b) vertical velocity, (c) total condensate mixing ratio, (d) buoyancy, (e) total vertical mass flux, (f) total convective mass flux sampled where vertical velocity is greater than 1 m s^{-1} , (g) total convective mass flux sampled where vertical velocity is greater than 2 m s^{-1} , (h) total downdraft vertical mass flux sampled where vertical velocity is less than -1 m s^{-1} , (i) the fraction of the domain satisfied by (e), (j) the fraction of the domain satisfied by (f), (k) the fraction of the domain satisfied by (g), (l) the fraction of the domain satisfied by (h), (m) net latent heating, (n) net latent heat of fusion, and (o) net latent heat of vaporization. The legend indicates the respective simulations of 2MOM, 1MM, 5MM, and 1CM.

near the freezing level in the midlevel updraft. The F_{RECIRC} is estimated to account for up to about 20%, 26%, 10%, and 0% of the net latent heating near the freezing level of the updraft for the 2MOM, 1MM, 5MM, and 1CM squall lines, respectively (Fig. 12). While the spatial extent of the region within the updraft that is most directly affected by F_{RECIRC} is not large, its

influence on squall-line intensity has been shown to be large, as it can act as a positive feedback mechanism. This is summarized as follows: 1) hail and rain are ingested into the midlevel updraft and help to invigorate vertical velocity through microphysically induced enhancement of buoyancy; 2) the increase in convective mass flux combined with the entrained hydrometeors

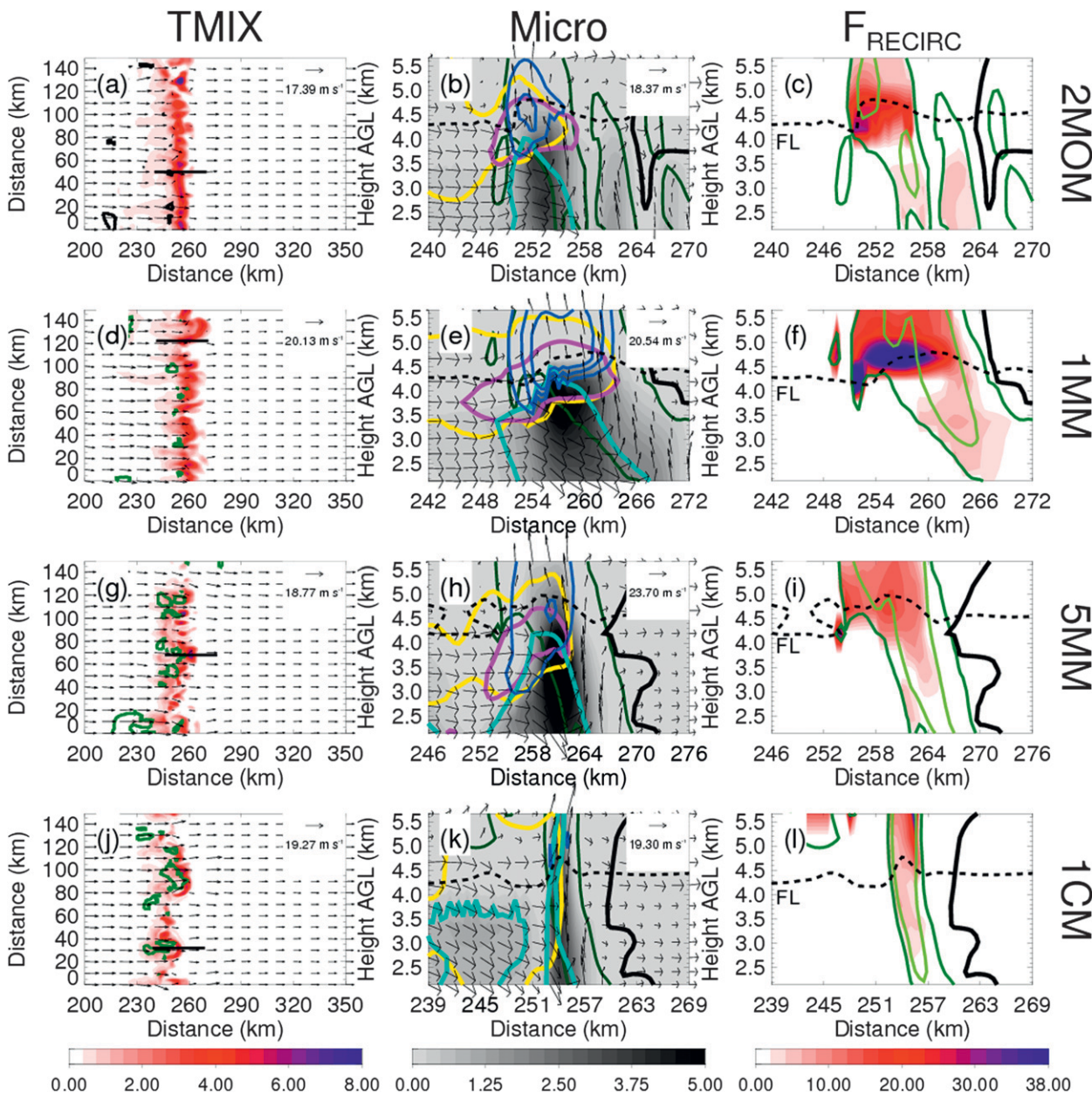


FIG. 11. (left) Plan-view cross sections of total condensate (shaded) and (middle),(right) vertical cross sections through the maximum value of 4-km-AGL total condensate: (a)–(c) 2MOM, (d)–(f) 1MM, (g)–(i) 5MM, and (j)–(l) 1CM. The location of each vertical cross section is depicted by the black horizontal line in (a),(d),(g), and (j). Rain mixing ratio (g kg^{-1} ; shaded), hail mixing ratio (0.5 g kg^{-1} ; blue contour), riming of rain by hail [$0.5 \text{ g kg}^{-1} (5 \text{ min})^{-1}$; yellow contour], net vapor deposition of hail [$0.05 \text{ g kg}^{-1} (5 \text{ min})^{-1}$; magenta contour], horizontal rain flux ($0.05 \text{ g m}^{-2} \text{ s}^{-1}$; light blue contour), U - W wind vectors, 1 m s^{-1} vertical velocity (dark green contour), the freezing level (dashed), and cloud boundary (thick black) are shown in (b),(e),(h), and (k). The recirculation heating fraction (shaded), 1 m s^{-1} (dark green contour) and 5 m s^{-1} (light green contour) vertical velocity, the freezing level (dashed), and cloud boundary (thick black) are shown in (c),(f),(i), and (l).

helps to loft more liquid condensate higher above the freezing level, potentially enhancing the latent heat released in association with freezing, thereby further enhancing buoyancy and increasing ice mass; 3) the increase in ice mass enhances convective downdrafts

that strengthen the cold pool and simultaneously enhance the low-level updrafts; and 4) the stronger updrafts enhance supersaturation and produce more condensate that further facilitates the recirculation mechanism.

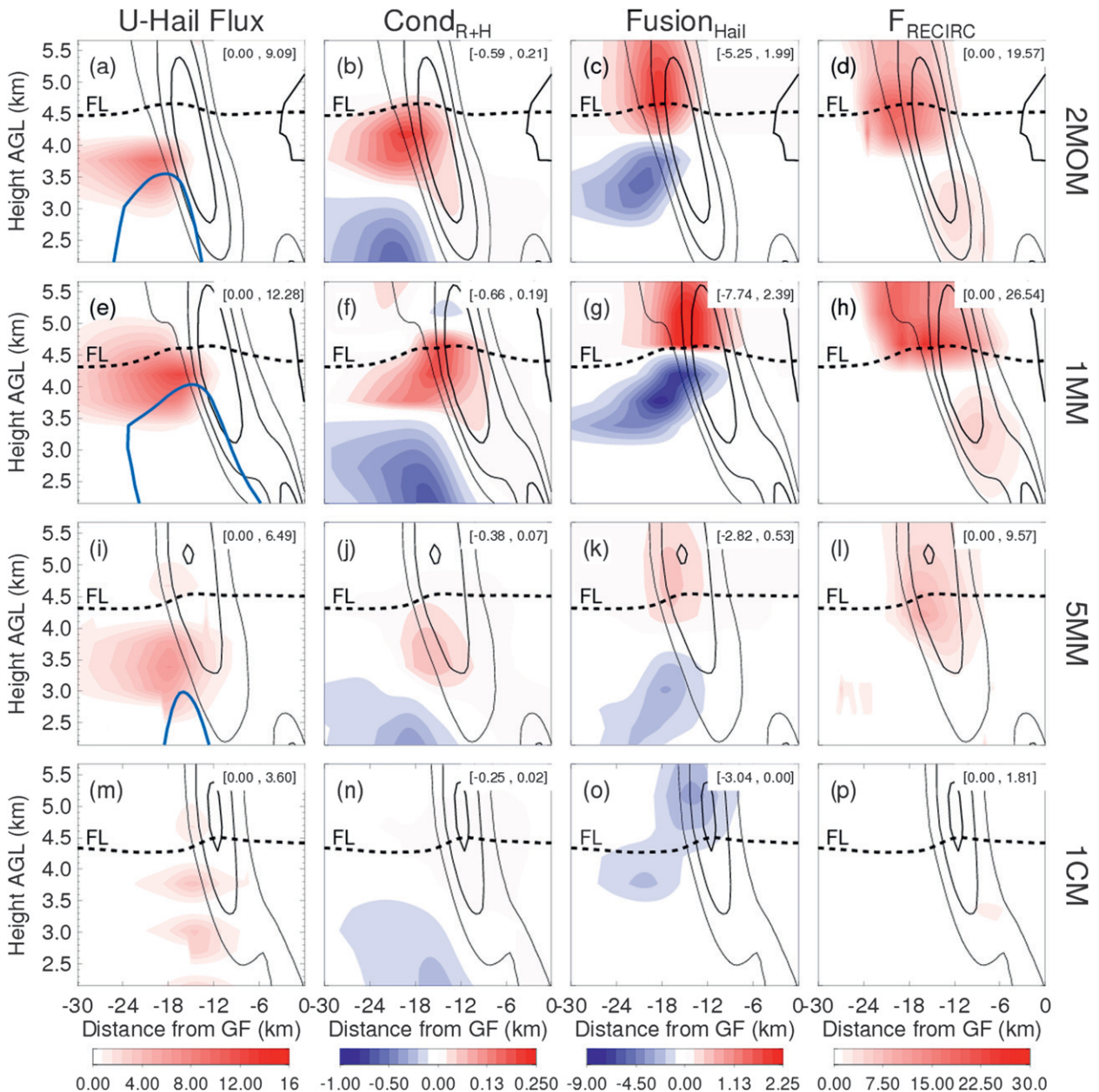


FIG. 12. Gust front and temporally averaged for (a)–(c) 2MOM, (d)–(f) 1MM, (g)–(i) 5MM, and (j)–(l) 1CM squall line from simulation hours 3–7. Each vertical cross section is expressed as a horizontal distance (x axis) from the gust front and a vertical distance AGL (y axis). The domain shown is centered over the recirculation mechanism and can be seen relative to the entire squall line in Fig. 8. The solid black contours in the center of each image are the 1, 2, and 3 m s^{-1} updraft regions, the dashed line is the freezing level, the thick black contour at the right edge of some images is cloud boundary, and the shaded contours are (a), (e), (i), (m) rear-to-front flux of hail condensate ($\text{g m}^{-2} \text{s}^{-1}$), (b), (f), (j), (n) net condensation of rain and hail averaged as 5-min differences ($\text{g kg}^{-1} 5 \text{ min}^{-1}$), (c), (g), (k), (o) net fusion of hail ($\text{g kg}^{-1} 5 \text{ min}^{-1}$), and (d), (h), (l), (p) net latent heating due to the recirculation mechanism [Eq. (2)]. The blue contours in (a), (e), (i), and (m) are the rear-to-front flux of rain condensate ($10 \text{ g m}^{-2} \text{s}^{-1}$).

5. Summary

Four simulations of an idealized squall line have been performed using RAMS that show the importance of a microphysical recirculation mechanism and its role in

aiding squall-line invigoration. First, a control simulation of a squall line using two-moment microphysics for all eight hydrometeor species showed the existence of a recirculation mechanism that begins with hail hydrometeors being ejected upshear from the main convective

updraft. As the hail hydrometeors descend below the freezing level, they encounter the RIJ of the squall line that advects them and melted rainwater back toward the midlevel updraft. The hail and rain become entrained into the upwind side of the updraft below the freezing level, where condensation and fusion onto the additional hail and rain hydrometeors promote extra latent heating that in turn enhances buoyancy.

As microphysics and dynamics in squall lines are intimately connected (Fovell and Ogura 1988; Ferrier et al. 1995; Adams-Selin et al. 2013a; Bryan and Morrison 2012), a sensitivity experiment was designed that would most effectively isolate the importance of the recirculation mechanism for squall lines. Three additional sensitivity simulations of a squall line were performed using single-moment microphysics in which the mean diameter of the hail hydrometeor distribution was varied. Analysis of the sensitivity experiments can be briefly summarized as follows:

- 1) $C/\Delta U$ ratios indicate that the squall lines are all near their maximum system intensity, while the mean squall-line propagation speed increases by up to about 10% as hail size decreases.
- 2) With smaller hail sizes, the vertical structure of the squall lines has a better-defined RIJ, stronger FTR flow, and stronger mesoscale updrafts and downdrafts.
- 3) As hail size decreases, precipitation increases along with TWP.
- 4) Both convective and total upward mass flux increase with smaller hail sizes.
- 5) Net latent heating, especially near the freezing level, increases with smaller hail sizes, leading to greater buoyancy.
- 6) The increased buoyancy near the freezing level can be attributed to a positive feedback between the recirculation mechanism and the cold pool, whereby the recirculation mechanism strengthens the midlevel updraft, which promotes increased frozen condensate that enhances the convective downdraft and strengthens the cold pool. The cold pool then enhances the low-level updraft and produces greater supersaturation and subsequent condensation, thereby facilitating the recirculation mechanism.

The experiments presented in this paper highlight the importance of the ice phase in numerically simulated squall lines. It is shown that through the recirculation mechanism, a stronger squall line can be sustained. While changes in cold pool intensity assist in strengthening the squall line, the greatest variations among the simulations occurred near the freezing level where the recirculation mechanism is present.

Acknowledgments. This work was jointly funded by the National Aeronautics and Space Administration under Grant NNX07AT11G and the National Science Foundation under Grant ATM-0820556. The authors wish to thank the three anonymous reviewers whose thoughtful comments were highly helpful in improving the content of this manuscript.

REFERENCES

- Adams-Selin, R. D., S. C. van den Heever, and R. H. Johnson, 2013a: Sensitivity of bow echo simulation to microphysical parameterizations. *Wea. Forecasting*, in press.
- , —, and —, 2013b: Impact of graupel parameterization schemes on idealized bow echo simulations. *Mon. Wea. Rev.*, **141**, 1241–1262.
- Anderson, C. J., and R. W. Arritt, 1998: Mesoscale convective complexes and persistent elongated convective systems over the United States during 1992 and 1993. *Mon. Wea. Rev.*, **126**, 578–599.
- Benjamin, T. B., 1968: Gravity currents and related phenomena. *J. Fluid Mech.*, **31**, 209–248.
- Brown, J. M., 1979: Mesoscale unsaturated downdrafts driven by rainfall evaporation: A numerical study. *J. Atmos. Sci.*, **36**, 313–338.
- Bryan, G. H., and M. D. Parker, 2010: Observations of a squall line and its near environment using high-frequency rawinsonde launches during VORTEX2. *Mon. Wea. Rev.*, **138**, 4076–4097.
- , and H. Morrison, 2012: Sensitivity of a simulated squall line to horizontal resolution and parameterization of microphysics. *Mon. Wea. Rev.*, **140**, 202–225.
- , J. C. Wyngaard, and J. M. Fritsch, 2003: Resolution requirements for the simulation of deep moist convection. *Mon. Wea. Rev.*, **131**, 2394–2416.
- , J. C. Knievel, and M. D. Parker, 2006: A multimodel assessment of RKW theory's relevance to squall-line characteristics. *Mon. Wea. Rev.*, **134**, 2772–2792.
- , R. Rotunno, and J. M. Fritsch, 2007: Roll circulations in the convective region of a simulated squall line. *J. Atmos. Sci.*, **64**, 1249–1266.
- Carbone, R. E., J. W. Conway, N. A. Crook, and M. W. Moncrieff, 1990: The generation and propagation of a nocturnal squall line. Part I: Observations and implications for mesoscale predictability. *Mon. Wea. Rev.*, **118**, 26–49.
- Coniglio, M. C., S. F. Corfidi, and J. S. Kain, 2012: Views on applying RKW Theory: An illustration using the 8 May 2009 derecho-producing convective system. *Mon. Wea. Rev.*, **140**, 1023–1043.
- Corfidi, S. F., 2003: Cold pools and MCS propagation: Forecasting the motion of downwind-developing MCSs. *Wea. Forecasting*, **18**, 997–1017.
- Cotton, W. R., and Coauthors, 2003: RAMS 2001: Current status and future directions. *Meteor. Atmos. Phys.*, **82**, 5–29.
- Dawson, D. T., M. Xue, J. A. Milbrandt, and M. K. Yau, 2010: Comparison of evaporation and cold pool development between single-moment and multimoment bulk microphysics schemes in idealized simulations of tornadic thunderstorms. *Mon. Wea. Rev.*, **138**, 1152–1171.
- DeMott, P. J., K. Sassen, M. R. Poelle, D. Baumgardner, D. C. Rogers, S. D. Brooks, A. J. Prenni, and S. M. Kreidenweis, 2003: African dust aerosols as atmospheric ice nuclei. *Geophys. Res. Lett.*, **30**, 1732, doi:10.1029/2003GL017410.
- Emanuel, K. A., 1994: *Atmospheric Convection*. Oxford University Press, 580 pp.

- Ferrier, B. S., W.-K. Tao, and J. Simpson, 1995: A double-moment multiple-phase four-class bulk ice scheme. Part II: Simulations of convective storms in different large-scale environments and comparisons with other bulk parameterizations. *J. Atmos. Sci.*, **52**, 1001–1033.
- Fierro, A. O., L. M. Leslie, E. R. Mansell, and J. M. Straka, 2008: Numerical simulations of the microphysics and electrification of the weakly electrified 9 February 1993 TOGA COARE squall line: Comparisons with observations. *Mon. Wea. Rev.*, **136**, 364–379.
- , J. Simpson, M. A. LeMone, J. M. Straka, and B. F. Smull, 2009: On how hot towers fuel the Hadley cell: An observational and modeling study of line-organized convection in the equatorial trough from TOGA COARE. *J. Atmos. Sci.*, **66**, 2730–2746.
- Flatau, P. J., G. J. Tripoli, J. Verlinde, and W. R. Cotton, 1989: The CSU-RAMS Cloud Microphysics Module: General theory and code documentation. Colorado State University Department of Atmospheric Science Paper 451, 88 pp.
- Fovell, R. G., and Y. Ogura, 1988: Numerical simulation of a mid-latitude squall line in two dimensions. *J. Atmos. Sci.*, **45**, 3846–3879.
- , and P.-H. Tan, 1998: The temporal behavior of numerically simulated multicell-type storms. Part II: The convective cell like cycle and cell regeneration. *Mon. Wea. Rev.*, **126**, 551–577.
- , G. L. Mullendore, and S.-H. Kim, 2006: Discrete propagation in numerically simulated nocturnal squall lines. *Mon. Wea. Rev.*, **134**, 3735–3752.
- Frame, J., and P. Markowski, 2006: The interaction of simulated squall lines with idealized mountain ridges. *Mon. Wea. Rev.*, **134**, 1919–1941.
- Gilmore, M. S., J. M. Straka, and E. N. Rasmussen, 2004: Precipitation and evolution sensitivity in simulated deep convective storms: Comparison between liquid-only and simple ice and liquid phase microphysics. *Mon. Wea. Rev.*, **132**, 1897–1916.
- Grim, J. A., R. M. Rauber, G. M. McFarquhar, and B. F. Jewett, 2009: Development and forcing of the rear inflow jet in a rapidly developing and decaying squall line during BAMEX. *Mon. Wea. Rev.*, **137**, 1206–1229.
- Haertel, P. T., and R. H. Johnson, 2000: The linear dynamics of squall line mesohighs and wake lows. *J. Atmos. Sci.*, **57**, 93–107.
- Harrington, J. Y., 1997: The effects of radiative and microphysical processes on simulated warm and transition season Arctic stratus. Ph.D. dissertation, Colorado State University, 289 pp.
- Hill, G. E., 1974: Factors controlling the size and spacing of cumulus clouds as revealed by numerical experiments. *J. Atmos. Sci.*, **31**, 646–673.
- Houze, R. A., Jr., 2004: Mesoscale convective systems. *Rev. Geophys.*, **42**, RG4003, doi:10.1029/2004RG000150.
- Jirak, I. L., W. R. Cotton, and R. L. McAnelly, 2003: Satellite and radar survey of mesoscale convective system development. *Mon. Wea. Rev.*, **131**, 2428–2449.
- Jorgensen, D. P., M. A. LeMone, and S. B. Trier, 1997: Structure and evolution of the 22 February 1993 TOGA COARE squall line: Aircraft observations of precipitation, circulation, and surface energy fluxes. *J. Atmos. Sci.*, **54**, 1961–1985.
- Klemp, J. B., and R. B. Wilhelmson, 1978: The simulation of three-dimensional convective storm dynamics. *J. Atmos. Sci.*, **35**, 1070–1096.
- Lafare, J.-P., and M. W. Moncrieff, 1989: A numerical investigation of the organization and interaction of the convective and stratiform regions of tropical squall lines. *J. Atmos. Sci.*, **46**, 521–544.
- Laing, A. G., and J. M. Fritsch, 1997: The global population of mesoscale convective complexes. *Quart. J. Roy. Meteor. Soc.*, **123**, 389–405.
- Lane, P. T., and M. W. Moncrieff, 2010: Characterization of momentum transport associated with organized moist convection and gravity waves. *J. Atmos. Sci.*, **67**, 3208–3225.
- Lebo, Z., and J. H. Seinfeld, 2011: Theoretical basis for convective invigoration due to increased aerosol concentration. *Atmos. Chem. Phys.*, **11**, 2179–2196.
- Lilly, D. K., 1962: On the numerical simulation of buoyant convection. *Tellus*, **14**, 148–172.
- Liu, C., M. W. Moncrieff, and E. J. Zipser, 1997: Dynamical influence of microphysics in tropical squall lines: A numerical study. *Mon. Wea. Rev.*, **125**, 2193–2210.
- Luo, Y., Y. Wang, H. Wang, Y. Zheng, and H. Morrison, 2010: Modeling convective-stratiform precipitation processes on a Mei-Yu front with the Weather Research and Forecasting model: Comparison with observations and sensitivity to cloud microphysics parameterizations. *J. Geophys. Res.*, **115**, D18117, doi:10.1029/2010JD013873.
- Matrosov, S. Y., 1999: Retrieval of vertical profiles of ice cloud microphysics from radar and IR measurements using tuned regressions between reflectivity and cloud parameters. *J. Geophys. Res.*, **104** (D14), 16 741–16 753.
- McCumber, M., W.-K. Tao, J. Simpson, R. Penc, and S.-T. Soong, 1991: Comparison of ice-phase microphysical parameterization schemes using numerical simulations of tropical convection. *J. Appl. Meteor.*, **30**, 985–1004.
- Meng, Z., F. Zhang, P. Markowski, D. Wu, and K. Zhao, 2012: A modeling study on the development of a bowing structure and associated rear inflow within a squall line over South China. *J. Atmos. Sci.*, **69**, 1182–1207.
- Meyers, M. P., R. L. Walko, J. Y. Harrington, and W. R. Cotton, 1997: New RAMS cloud microphysics parameterization. Part II: The two-moment scheme. *Atmos. Res.*, **45**, 3–39.
- Moncrieff, M. W., and C.-H. Liu, 1999: Convection initiation by density currents: Role of convergence, shear, and dynamical organization. *Mon. Wea. Rev.*, **127**, 2455–2464.
- Morrison, H., 2012: On the robustness of aerosol effects on an idealized supercell storm simulated with a cloud system-resolving model. *Atmos. Chem. Phys. Discuss.*, **12**, 10 493–10 533, doi:10.5194/acpd-12-10493-2012.
- , G. Thompson, and V. Tatarskii, 2009: Impact of cloud microphysics on the development of trailing stratiform precipitation in a simulated squall line: Comparison of one- and two-moment schemes. *Mon. Wea. Rev.*, **137**, 991–1007.
- , S. Tessendorf, K. Ikeda, and G. Thompson, 2012: Sensitivity of a simulated midlatitude squall line to parameterization of raindrop breakup. *Mon. Wea. Rev.*, **140**, 2437–2460.
- Newton, C. W., 1950: Structure and mechanism of the prefrontal squall line. *J. Meteor.*, **7**, 210–222.
- Nicholls, M. E., 1987: A comparison of the results of a two-dimensional numerical simulation of a tropical squall line with observations. *Mon. Wea. Rev.*, **115**, 3055–3077.
- Noppel, H., U. Blahak, A. Seifert, and K. D. Beheng, 2010: Simulations of a hailstorm and the impact of CCN using an advanced two-moment cloud microphysical scheme. *Atmos. Res.*, **96**, 286–301.
- Parker, M. D., and R. H. Johnson, 2000: Organizational modes of midlatitude mesoscale convective systems. *Mon. Wea. Rev.*, **128**, 3413–3436.
- Pielke, R. A., and Coauthors, 1992: A comprehensive meteorological modeling system—RAMS. *Meteor. Atmos. Phys.*, **49**, 69–91.

- Rotunno, R., J. B. Klemp, and M. L. Weisman, 1988: A theory for strong, long-lived squall lines. *J. Atmos. Sci.*, **45**, 463–485.
- Saleeby, S. M., and W. R. Cotton, 2004: A large-droplet mode and prognostic number concentration of cloud droplets in the Colorado State University Regional Atmospheric Modeling System (RAMS). Part I: Module descriptions and supercell test simulations. *J. Appl. Meteor.*, **43**, 182–195.
- Schmidt, J. M., and W. R. Cotton, 1990: Interactions between upper and lower tropospheric gravity waves on squall line structure and maintenance. *J. Atmos. Sci.*, **47**, 1205–1222.
- Seigel, R. B., and S. C. van den Heever, 2012a: Simulated density currents beneath embedded stratified layers. *J. Atmos. Sci.*, **69**, 2192–2200.
- , and —, 2012b: Dust lofting and ingestion by supercell storms. *J. Atmos. Sci.*, **69**, 1453–1473.
- Smagorinsky, J., 1963: General circulation experiments with the primitive equations. I. The basic experiment. *Mon. Wea. Rev.*, **91**, 99–164.
- Smull, B. F., and R. A. Houze Jr., 1987: Rear inflow in squall lines with trailing-stratiform precipitation. *Mon. Wea. Rev.*, **115**, 2869–2889.
- Stensrud, D. J., M. C. Coniglio, R. P. Davies-Jones, and J. S. Evans, 2005: Comments on “A theory for strong long-lived squall lines” revisited.” *J. Atmos. Sci.*, **62**, 2989–2996.
- Storer, R. L., S. C. van den Heever, and G. L. Stephens, 2010: Modeling aerosol impacts on convective storms in different environments. *J. Atmos. Sci.*, **67**, 3904–3915.
- Szeto, K. K., and H. Cho, 1994: A numerical investigation of squall lines. Part III: Sensitivity to precipitation processes and the Coriolis force. *J. Atmos. Sci.*, **51**, 1341–1351.
- Takemi, T., and T. Satomura, 2000: Numerical experiments on the mechanisms for the development and maintenance of long-lived squall lines in dry environments. *J. Atmos. Sci.*, **57**, 1718–1740.
- Tao, W.-K., J. R. Scala, B. Ferrier, and J. Simpson, 1995: The effect of melting processes on the development of a tropical and a midlatitude squall line. *J. Atmos. Sci.*, **52**, 1934–1948.
- Thorpe, A. J., M. J. Miller, and M. W. Moncrieff, 1982: Two-dimensional convection in non-constant shear: A model of midlatitude squall lines. *Quart. J. Roy. Meteor. Soc.*, **108**, 739–762.
- Tompkins, A. M., 2001: Organization of tropical convection in low vertical wind shears: The role of cold pools. *J. Atmos. Sci.*, **58**, 1650–1672.
- Trier, S. B., W. C. Skamarock, and M. A. LeMone, 1997: Structure and evolution of the 22 February 1993 TOGA COARE squall line: Organization mechanisms inferred from numerical simulations. *J. Atmos. Sci.*, **54**, 386–407.
- Tulet, P., K. Crahan-Kaku, M. Leriche, B. Aouizerats, and S. Crumeyrolle, 2010: Mixing of dust aerosols into a mesoscale convective system: Generation, filtering and possible feedbacks on ice anvils. *Atmos. Res.*, **96**, 302–314.
- van den Heever, S. C., and W. R. Cotton, 2004: The impact of hail size on simulated supercell storms. *J. Atmos. Sci.*, **61**, 1596–1609.
- , G. G. Carrió, W. R. Cotton, P. J. DeMott, and A. J. Prenni, 2006: Impacts of nucleating aerosol on Florida storms. Part I: Mesoscale simulations. *J. Atmos. Sci.*, **63**, 1752–1775.
- , G. L. Stephens, and N. B. Wood, 2011: Aerosol indirect effects on tropical convection characteristics under conditions of radiative–convective equilibrium. *J. Atmos. Sci.*, **68**, 699–718.
- Van Weverberg, K., A. Vogelmann, H. Morrison, and J. Milbrandt, 2012: Sensitivity of idealized squall line simulations to the level of complexity used in two-moment bulk microphysics schemes. *Mon. Wea. Rev.*, **140**, 1883–1907.
- Verlinde, J., P. J. Flatau, and W. R. Cotton, 1990: Analytical solutions to the collection growth equation: Comparison with approximate methods and application to cloud microphysics parameterization schemes. *J. Atmos. Sci.*, **47**, 2871–2880.
- Walko, R. L., C. J. Trempack, R. A. Pielke, and W. R. Cotton, 1995: An interactive nesting algorithm for stretched grids and variable nesting ratios. *J. Appl. Meteor.*, **34**, 994–999.
- , and Coauthors, 2000: Coupled atmosphere–biophysics–hydrology models for environmental modeling. *J. Appl. Meteor.*, **39**, 931–944.
- Ward, D., and W. R. Cotton, 2011: A method for forecasting cloud condensation nuclei using predictions of aerosol physical and chemical properties from WRF/Chem. *J. Appl. Meteor. Climatol.*, **50**, 1601–1615.
- Weisman, M. L., 1992: The role of convectively generated rear-inflow jets in the evolution of long-lived mesoconvective systems. *J. Atmos. Sci.*, **49**, 1826–1847.
- , 1993: The genesis of severe, long-lived bow echoes. *J. Atmos. Sci.*, **50**, 645–670.
- , and J. B. Klemp, 1982: The dependence of numerically simulated convective storms on vertical wind shear and buoyancy. *Mon. Wea. Rev.*, **110**, 504–520.
- , and R. Rotunno, 2004: “A theory for strong long-lived squall lines” revisited. *J. Atmos. Sci.*, **61**, 361–382.
- , and —, 2005: Reply. *J. Atmos. Sci.*, **62**, 2997–3002.
- , J. B. Klemp, and R. Rotunno, 1988: Structure and evolution of numerically simulated squall lines. *J. Atmos. Sci.*, **45**, 1990–2013.
- Xiao, Q., and J. Sun, 2007: Multiple-radar data assimilation and short-range quantitative precipitation forecasting of a squall line observed during IHOP_2002. *Mon. Wea. Rev.*, **135**, 3381–3404.
- Xue, M., 2002: Density currents in shear flows: Effects of rigid lid and cold-pool internal circulation, and application to squall line dynamics. *Quart. J. Roy. Meteor. Soc.*, **128**, 47–73.